

Double-peaked narrow emission-line galaxies from Sloan Digital Sky Survey.

I. Sample and basic properties

Jun-Qiang Ge¹, Chen Hu¹, Jian-Min Wang^{1,2,*}, Jin-Ming Bai³ and Shu Zhang¹

ABSTRACT

Recently, much attention has been given to double-peaked narrow emission-line galaxies, some of which are suggested to be related with merging galaxies. We make a systematic search to build the largest sample of these sources from Data Release 7 of Sloan Digital Sky Survey (SDSS DR7). With reasonable criteria of fluxes, full-width-half-maximum of emission lines and separations of the peaks, we select 3,030 double-peaked narrow emission-lines galaxies. In light of the existence of broad Balmer lines and the locations of the two components of double-peaked narrow emission lines distinguished by the Kauffmann et al. (2003) criteria in the Baldwin-Phillips-Terlevich (BPT) diagram, we find that there are 81 type I AGN, 837 double-type II AGN (2-type II), 708 galaxies with double star forming components (2-SF), 400 with mixed star forming and type II AGN components (type II + SF) and 1,004 unknown-type objects. As a by-product, a sample of galaxies (12,582) with asymmetric or top-flat profiles of emission lines is established. After inspecting the SDSS images of the two samples visually, we find 54 galaxies with dual cores. The present samples can be used to study the dynamics of merging galaxies, the triggering mechanism of black hole activity, the hierarchical growth of galaxies and dynamics of narrow line regions driven by outflows and rotating disk.

Subject headings: black hole physics — galaxies: evolution

1. Introduction

Double-peaked narrow emission-line active galactic nuclei (hereafter *pp*-AGNs) have been found since the 1980s (e.g. Heckman et al. 1981, 1984; Keel 1985; Whittle 1985a,b,c), but were mainly interpreted as an indicator of outflows from active nuclei or rotating narrow line regions (e.g. Greene & Ho 2005). Since the suggestion that double-peaked profiles could be produced by dual AGN (Zhou

¹ Key Laboratory for Particle Astrophysics, Institute of High Energy Physics, Chinese Academy of Sciences, 19B Yuquan Road, Beijing 100049, China

² National Astronomical Observatories, Chinese Academy of Sciences, 20 Datun Road, Beijing 100020, China

³Yunnan Observatory, Chinese Academy of Sciences, Kunming 650011, China

*Corresponding author: wangjm@mail.ihep.ac.cn

et al. 2004; Wang et al. 2009), much attention has been recently paid to search for individual objects and study statistical properties of *pp*-AGNs samples in light of several fundamental issues related with evolution of galaxies and AGN (for a summary of previous works on this subject see Table 1). There are 8 individual objects with double-peaked narrow emission-line profiles in total listed in Table 1, and three samples that made systematic searches for *pp*-AGNs from SDSS DR7 (Wang et al. 2009; Liu et al. 2010a; Smith et al. 2010; hereafter W09, L10 and S10, respectively). W09, L10 and S10 select their samples by employing different selection criteria, including restricting equivalent width (EW), redshift, signal-to-noise ratio (S/N), narrow emission line (NEL) flux ratio etc. W09 and L10 select 190 *pp*-AGNs in total from SDSS galaxy sample using Kewley et al. (2001) criterion in the BPT diagram (Baldwin et al. 1981). This paper applies new selection scheme and criteria to hunt double-peaked narrow emission-line galaxies (*pp*-galaxies) from $\sim 920,000$ galaxies.

Double-peaked narrow line profiles can be caused by different mechanisms discussed subsequently. First, bi-polar outflows driven by starbursts or AGN radiation pressure have been suggested for many years, especially in several individual objects, such as NGC 1068 (Crenshaw & Kraemer 2000; Das et al. 2006, 2007), NGC 4151 (Huchings et al. 1998; Crenshaw et al. 2000; Das et al. 2005), Mrk 3 (Ruiz et al. 2001; Crenshaw et al. 2010a), Mrk 78 (Fisher et al. 2011), and Mrk 573 (Schlesinger et al. 2009; Fisher et al. 2010). In particular, outflows can produce double-peaked (e.g. Mrk 78 see Fisher et al. 2011) or multiple-peaked emission-line profiles (e.g. NGC 1068, see also Crenshaw et al. 2010b) depending on the projection of the outflows in the line of sight. However, W09 found an anti-correlation between the flux (F_r/F_b) and shift ($\Delta\lambda_r/\Delta\lambda_b$) ratios of the double peaks, where F and $\Delta\lambda$ are the fluxes and shifts of red and blue components, which has been confirmed by Liu et al. (2010a, see their Figure 6e), Smith et al. (2010, see their Figure 5) and Fu et al. (2011, see their Figure 5). This new statistical relation strongly suggests co-rotating dual AGN model. Unless the bi-polar outflows with very asymmetric mass rates are under momentum conservation, the anti-correlation would not favor the presence of bi-polar outflows (W09)¹. Second, rotating disk-like narrow line regions (NLRs) with circular orbits are *not* able to produce the anti-correlation because a large fraction of *pp*-AGNs have $F_r/F_b \neq 1$, unless the rotating NLRs have complicated elliptical orbits (or inhomogeneous mass distribution over the rotating disk) and orientations to observers. Third, the origin of double-peaked profiles could be interpreted by dual AGN which will be in agreement with the anti-correlation (W09; L10; Smith et al. 2010; Rosario et al. 2011) as identified by some works (e.g. Fu, et al. 2011; Shen, et al. 2011) listed in Table 1. In order to identify the nature of these *pp*-AGN, near infrared (NIR) images and optical long slit spectroscopy have shown that about 50% type I *pp*-AGN (Fu et al. 2011), 10-20% type II *pp*-AGN (Liu et al. 2010b; Shen et al. 2011; Fu et al. 2011, 2012), or more than 50% *pp*-AGNs (Comerford et al. 2011) and 50% double-peaked quasars (Rosario et al. 2011) have two cores. The nature of the remaining objects is open (a single core: bi-polar outflows or rotating NLR; or spatially unresolved dual-cores).

¹Here we assume that the outflows are optically thin. The radiation from them is proportional to the mass of the emitting gas expected.

Double-peaked narrow emission-line galaxies play an important role in studies of the dynamics of AGN NLRs and merging galaxies. The formation of NLRs is insufficiently understood even though they are spatially resolved in some individual objects (Bennert et al. 2002; Schmitt et al. 2003; Bennert et al. 2006a,b). Jet-induced outflows are responsible for NLR formation in some AGN (Bicknell et al. 1998) in light of individual objects, such as Mrk 3 (Capetti et al. 1999), and Mrk 78 (Whittle & Wilson 2004). More clear evidence for the jet-clouds interaction in NGC 4051 has been revealed by *Chandra* (Wang et al. 2011). Cold clouds are formed by the cocoons produced through the Kelvin-Helmholtz instability of the relativistic jet propagating in the interstellar medium (ISM) (Steffen et al. 1997). NLRs driven by the intermediate scale of outflows or jets can cause the appearance of double-peaked profiles (Rosario et al. 2008, 2010). This is supported by the fact that there is a correlation between the jet power and width of NELs (Wilson & Willis 1980) and powerful, compact linear radio sources have anomalously broad [O III] lines usually (Whittle 1992). It remains to be systematically researched on NLR dynamics driven by jet-induced outflows in a large and homogeneous sample. Furthermore, feedback to starburst through AGN outflows is presumed to play a key role in regulating bulge growth, but it still needs to be evidenced by observations of a large *pp*-galaxies sample driven by bi-polar outflows. On the other hand, Greene & Ho (2005) conducted a systematic investigation of NLR dynamics from a large SDSS sample. They draw a conclusion that the NLR is mainly governed by the potential of bulges though there are some evidence for rotation-supported NLR in light of Integral Field Unit (IFU) rotation curves (Vega Beltrán et al. 2001; Dumas et al. 2007; Stoklasová et al. 2009). Clearly, those *pp*-AGNs with double-peaked NELs produced by a rotation-supported NLR would be used to justify if the rotation-supported NLR follows the dynamics of bulges (Dumas et al. 2007; Ho 2009) or the rotation of partial disks of galaxies, even provide an opportunity to study the relative orientation of AGN and host galaxies (Shen et al. 2010; Lagos et al. 2011).

Merging galaxies enter a special phase in which double cores exist after their galactic disks merge within the framework of the theory of hierarchical galaxy formation and evolution (e.g. Longair 2008; Yu et al. 2011). As illustrated by SDSS images (e.g. Figure 2 in Darg et al. 2010), there is a sequence of galaxy mergers from tidal interaction between two galaxies with a separation of tens of kpc to an “approaching post-merger” stage containing dual cores with a \sim kpc separation. If hierarchical growth of galaxies works, are there AGN-starburst cores, or galaxies with dual starbursts? How often? Do they appear as *pp*-galaxies? If so, these *pp*-galaxies could open a new clue to understanding the issues related to triggering starbursts and black hole activity, and help to understand the details of mergers. Second, dual-cored galaxies are important for the subject of black hole binaries searched through shifts between broad lines and narrow lines (Tsalmantza et al. 2011, Eracleous et al. 2011) since dual-cored galaxies are progenitors of binary black holes. With the dual-cored galaxies, we will have an entire scenario of merging process. These motivate us to systematically search for *pp*-galaxies to look into statistical properties.

In this paper, we make an attempt to establish the largest sample of *pp*-galaxies through a systematical search from SDSS DR7 spectra. As a by-product, we also build a sample of asymmetric

or top-flat narrow line (asym-NEL) galaxies, some of which could be candidates of *pp*-galaxies. Section 2 describes the followed procedures, selection criteria and the final samples of this work. We systematically inspect images of the *pp*-galaxies and asym-NEL galaxies in Section 3 and find 54 of them with dual cores. In Section 4, we present the basic properties of the sample. We draw conclusions in Section 5. We use a standard cosmology with $H_0 = 71 \text{ km s}^{-1} \text{ Mpc}^{-1}$, $\Omega_M = 0.27$ and $\Omega_\Lambda = 0.73$ in this paper.

2. Sample Selection

For the goal of selecting *pp*-galaxies, we develop a series of automatic algorithms in light of Monte-Carlo simulations given by the Appendix A. We apply the algorithms to SDSS galaxy spectra and get candidates of the *pp*-galaxies. Then we visually inspect the candidate spectra to establish the final sample. We follow the procedures: (1) select emission-line galaxies from the entire sample of galaxies spectroscopically observed by SDSS; (2) pure emission-line spectra are created by subtracting stellar components using spectral synthesis methods; (3) *F*-test is employed to examine whether double-Gaussians are needed to fit each NEL in individual objects, if so, they are selected as candidates of *pp*-galaxies; (4) finally, we visually inspect spectra of the candidates and establish the final sample. We classify the sample into sub-samples according to the width of their broad Balmer emission lines and NEL ratios using the BPT diagram (Baldwin et al. 1981). Figure 1 shows a brief flowchart of the whole procedures which are described in detail below.

2.1. Emission-line spectra of galaxies

We start from the database of the MPA-JHU² SDSS DR7 galaxy sample (in total 927,552 galaxy spectra; Abazajian et al. 2009). First, 737,824 sources are selected from those with a signal-to-noise ratio $S/N > 9$ based on the results by L10³ in the rest-frame wavelength range 4800-5100Å. Second, 337,188 emission-line galaxies are selected from the 737,824 sources in light of that at least one of $H\alpha$, $[O \text{ III}] \lambda 5007$ and $H\beta$ lines has equivalent width greater than 3Å (Hao et al. 2005).

Measurement accuracy of redshifts of galaxies is very important to investigate properties of *pp*-galaxies. In this work, we measure cosmological redshifts (z) of the galaxy absorption lines (i.e. Ca II H+K and Mg Ib triplets) using the direct pixel-fitting method following Greene & Ho (2006) and Ho et al. (2009). The stellar templates used here are selected from the Indo-U.S. Library of Coudé Feed Stellar Spectra (Valdes et al. 2004, hereafter V04). The original dispersion of these

²The MPA/JHU catalog can be downloaded from <http://www.mpa-garching.mpg.de/SDSS/DR7>. We use $H\alpha$, $[O \text{ III}]$ and $H\beta$ measurements of the MPA sample.

³It should be noted that $S/N > 5$ is employed by L10 as a selection criterion (see Table 1), but their resultant *pp*-AGNs actually all have $S/N > 9$. Hence we use $S/N > 9$ in this paper.

spectrum templates is 0.4\AA , and a resolution of 1\AA full-width-half-maximum (FWHM), which are suitable for applying to SDSS data (i.e. $\delta z/z = \delta V_{\text{SDSS}}/c \sim 2 \times 10^{-4}$, where δz is the accuracy of the measured z and $\delta V_{\text{SDSS}} \sim 70\text{km s}^{-1}$ is the spectral resolution of SDSS).

We simultaneously obtain velocity dispersion (σ_*) of galaxies and redshift correction (Δz) from fitting the absorption line systems of the host galaxies by direct-pixel fitting method. Bernardi et al. (2003) show in detail that the 4000-7000 \AA is the best window for σ_* in their SDSS sample of elliptical galaxies, however, this window could be not the best one for Δz . We search reasonable windows for both σ_* and Δz , and find the 3800-7000 \AA is the best window since the mean values of χ^2 are the minimum in our present sample. We find $\langle \chi^2 \rangle = 1.2$ for 4000-7000 \AA whereas $\langle \chi^2 \rangle = 1.1$ for 3800-7000 \AA . In the meanwhile, σ_* values are consistent with each other for the 3800-7000 \AA and 4000-7000 \AA windows (we find that the difference of dispersion velocity, $\langle \delta \sigma_* \rangle \approx 9 \pm 19\text{km s}^{-1}$, and $\langle \delta V \rangle \approx 8 \pm 11\text{km s}^{-1}$, both difference could be neglected, where $\delta V = \delta(\Delta z)c$). Therefore, we select the 3800-7000 \AA window mainly by justifying $\langle \chi^2 \rangle$ for the sample in this paper.

An example of the galactic spectra fitted with stellar templates is shown in Figure 2 *top-left* panel, and the χ^2 -distributions of the fittings of the sample in Figure 2 *top-right*. We find that the χ^2 distribution of the fits in the restricted ranges is better than the ones for the fits in the full spectral band. This means that the direct pixel-fitting method only applies to determine the redshifts of galaxies through absorption lines, rather than estimating the underlying continuum. Stellar velocity dispersions are measured mainly through Ca II H+K and Mg Ib absorption lines. We have examined if there are some sources with double systems of absorption lines, but no sources are found in the sample⁴. Cosmological redshifts of *all* emission-line galaxies are determined by this method in the present paper.

Using STARLIGHT (Cid Fernandes et al. 2005), we estimate the underlying continuum. This code employs 45 stellar population templates (i.e. Base.BC03.N) which are composed of 3 metallicities and 15 ages (Bruzual & Charlot 2003, hereafter BC03). We make correction for Galactic extinction (Cardelli et al. 1989) and redshift. Since the BC03 template spectra have a homogeneous wavelength interval of 1\AA , we have to interpolate SDSS spectra to the same interval with the templates⁵. STARLIGHT is used to fit the interpolated spectra and to get stellar absorption and continuum spectra (SACS) of galaxies. Figure 2 *bottom-left* shows an example of the fit, whereas the *right* panel shows the χ^2 -distribution of the fittings for the sample. Comparing the χ^2 -distributions presented in Figure 2 *bottom-right*, we find that applications of STARLIGHT to the whole spectral coverage are better than to the restricted regions (see caption of Figure 2). Though STARLIGHT

⁴We also checked the 54 dual-cored galaxies given in Section 3, but they do not show double systems of absorption lines either. The reasons for this phenomenon remain open. It may result from the complicated situation of merging galaxies, in which the NLR dynamics does not follow the merging galaxies. Clearly, it is worth of observing the 54 dual-cored *pp*-galaxies from the present sample through long-slit spectroscopy.

⁵The sampling SDSS spectra of $\Delta \log \lambda = 10^{-4}$ gives $\delta \lambda \approx 1.15\text{\AA}$ at 5007\AA , implying that the interpolated spectra are accurate enough.

provides redshifts of galaxies, its results seem to be less accurate than the ones obtained with the direct pixel-fitting method (see Figure 2 *top-, bottom-right*). These comparisons show that the STARLIGHT applies to estimate the underlying continuum whereas the direct pixel-fitting method to determine the redshifts and stellar velocity dispersion.

We interpolate the SACS to the SDSS spectral points, and obtain pure emission-line spectra from SDSS spectra by subtracting the interpolated SACS. Errors of the data points in the pure emission line spectra are taken as the same as that in the SDSS original spectra. The pure emission-line spectra are employed to determine the shifts and the fluxes of the double peaks.

Finally, we note that the subtraction of Balmer absorption lines could make some artificial broad components though it is examined by χ^2 . In practice it turns out that the artificial components are produced if the AGN components are relatively brighter than their hosts, especially in some type I *pp*-AGNs with $\chi^2 > 1.5$. Fortunately, the fraction of these galaxies is less than $\sim 1\%$.

2.2. Analysis of emission-line spectra

The pure emission-line spectra may contain several kinetic components of emission lines as shown in Figure 3: narrow lines ([N II], [O III] H α , H β), [O III] wings (usually blueshifted, but sometimes redshifted), broad Balmer emission lines. We fit the lines with several Gaussian components, and classify them into different groups in light of kinetics. In each group, every Gaussian has the same shift and width. The pure emission-line spectra are modeled by (1) one or two groups for the NELs (narrow Gaussian group) corresponding to a single or double peaks; (2) one group for [O III] $\lambda\lambda$ 4959, 5007 wings, respectively ([O III] wing group); (3) one group for broad H α and H β components (broad Balmer group). We stress that the group components of each model are independent, in particular the widths, the shifts and the fluxes of the [O III] wings are free in the fittings. Except for the intensity ratios of [O III] λ 5007/ λ 4959 = 3 and [N II] λ 6584/ λ 6548 = 3 (Osterbrock & Ferland 2006), all line fluxes are set free.

There are eight models with different combinations of groups as shown in Table 2. We fit each individual spectrum with all of the eight models and calculate χ^2 in three wavelength bands: χ_β^2 for [O III] and H β fitting in the rest-frame wavelength range 4770-5080Å, χ_α^2 for [N II] and H α fitting in the range 6400-6700Å, and χ_t^2 for fitting in the two ranges simultaneously. For galaxies with $z > 0.39$, only χ_β^2 is available. After obtaining the χ^2 of all the eight models, we use *F*-test (Lupton 1993, Chap. 12.1) to determine the best model for each sources through three quantities defined as

$$f_\alpha = \frac{\chi_{\alpha_1}^2/n_{\alpha_1}}{\chi_{\alpha_2}^2/n_{\alpha_2}}, \quad f_\beta = \frac{\chi_{\beta_1}^2/n_{\beta_1}}{\chi_{\beta_2}^2/n_{\beta_2}}, \quad f_t = \frac{\chi_{t_1}^2/n_{t_1}}{\chi_{t_2}^2/n_{t_2}}. \quad (1)$$

where f_α , f_β and f_t follow F_α -, F_β - and F_t -distribution. We take the minimum probability $P_{\min} = \min(P_\alpha, P_\beta, P_t)$, where P_α, P_β, P_t are the probabilities defined as

$$P_\alpha = P(F > F_\alpha), \quad P_\beta = P(F > F_\beta), \quad P_t = P(F > F_t). \quad (2)$$

These probabilities are used to check whether the model with more Gaussians can improve the fitting in the corresponding wavelength range. If $1 - P_{\min} > 99.73\%$ (3σ), then the model with more Gaussians is considered to be better. Such comparisons are done between the eight models, from the simplest one to those with more and more Gaussians, until a model with more Gaussians can not improve the fitting. We then reach the best model for all individual objects. After directly removing those sources with a single Gaussian group from the best model, we are left with 118,871 sources with double narrow Gaussian groups (model M2, M6, M7 or M8).

Since the reliability of F -test mainly depends on the S/N ratio, the intensity ratio of the narrow lines and the confidence level, some sources with a single Gaussian group are incorrectly identified by the above F -test as sources with red and blue components. We choose a low confidence level in order to avoid losing any candidates, however, we proceed to remove those pseudo candidates according to the following empirical criterion. We employ the conservative criteria as

$$0.03 < F_r/F_b < 30.0, \quad (3)$$

$$\sigma_{\text{err,red}}/\sigma_{\text{red}} < 0.2, \quad \sigma_{\text{err,blue}}/\sigma_{\text{blue}} < 0.2, \quad (4)$$

where F_r and F_b are fluxes of red and blue components respectively, σ_{red} and σ_{blue} are the corresponding velocity dispersions, while $\sigma_{\text{err,red}}$ and $\sigma_{\text{err,blue}}$ are their errors. These empirical criteria guarantee that the NELs do need two-Gaussians under the signal-to-noise ratio of SDSS spectra. Otherwise, one of the two Gaussian components will be overwhelmed with spectral noise (see Appendix A). With conditions (3) and (4), we identify 107,745 sources which require two Gaussians to fit their NELs. In the next subsection, we use the parameters of the two Gaussians to obtain candidates with double-peaked and asym-NEL galaxies.

2.3. Final sample of pp -galaxies

A profile composed of two narrow Gaussian components shows double peaks when the separation of the two components is large enough. Using Monte-Carlo simulations (see Appendix A for details), we find the following criteria useful for selecting candidates with double-peaked profiles:

$$\Delta V/\text{FWHM}_{\min} > 0.8, \quad \text{or} \quad \Delta V > 200\text{km s}^{-1}, \quad (5)$$

where ΔV is the relative velocity shift between the two narrow Gaussian components, $\text{FWHM}_{\min} = \min(\text{FWHM}_{\text{red}}, \text{FWHM}_{\text{blue}})$, FWHM_{red} and $\text{FWHM}_{\text{blue}}$ are FWHMs of two components respectively. After applying the criteria presented in equation (5), we obtain 42,927 candidates of pp -galaxies. As analyzed in Appendix A, the above procedures efficiently exclude those single-peaked galaxies and make it possible to select real pp -galaxies through visual inspection of spectra, but they are mixed with asym-NEL galaxies.

We visually inspect the 42,927 galaxies, and find that there are 3,030 pp -galaxies. As a by-product of the present criteria, we find 12,582 asym-NEL galaxies. The pp -galaxies are defined by

the fact that there is a clear “trough” in the profiles of narrow emission lines. We select asym-NEL galaxies, which do not show “trough”, and directly excluded those objects without strong asymmetric profiles. As we show in the Appendix A, the double-peaked sources are complete by making use of the present criteria, but asym-NEL sources are unavoidably selected. We point out that selection criteria of asym-NEL sources rule out many potential sources (see Appendix A) so that the selected sample is not complete. However the selected sources are still numerous up to 12,000, it is thus believed that statistical properties of the sample are meaningful. As we show in subsequent sections, the *pp*-galaxies and the asym-NEL galaxies follow similar statistic properties. Table 3 and 4 list all the *pp*-galaxies and asym-NEL galaxies as well as the widths, the fluxes, the redshifts and the blueshifts of the two peaks. The two tables are organized by object type (see Section 2.4).

2.4. Classification of the sample

Since the production of the red and blue peaks could be driven by different radiation mechanisms, we diagnose the nature of each peak components through the BPT diagram (Baldwin et al. 1981). Generally, the ratios of the narrow lines are probes of the nature of the ionizing sources, which are either young stars in star-forming (SF) regions or active galactic nuclei. If a galaxy has obvious broad components of Balmer lines ($H\alpha$ and $H\beta$), it should have at least one type I AGN component. The criteria for the type I AGN follows Hao et al. (2005):

$$\text{FWHM}(H\alpha) > 1200\text{km s}^{-1} \quad \text{and} \quad h_{H\alpha,\text{broad}}/\bar{h}_{H\alpha,\text{narrow}} > 0.1, \quad (6)$$

or

$$\text{FWHM}(H\alpha) > 2200\text{km s}^{-1}, \quad (7)$$

where $\bar{h}_{H\alpha,\text{narrow}} = (h_{H\alpha,\text{red}} + h_{H\alpha,\text{blue}})/2$ is the mean height of specific flux of the blue ($h_{H\alpha,\text{blue}}$) and red ($h_{H\alpha,\text{red}}$) narrow component of $H\alpha$. $\text{FWHM}(H\alpha)$ is the full-width-half-maximum of the broad $H\alpha$ component.

Figure 4 shows the BPT diagram of the red and the blue components of the present sample. The demarcation described in equation 1 of Kauffmann et al. (2003) is used to distinguish AGN and SF components in the BPT diagram. Several combinations are displayed in Figure 4: two type I AGN⁶; one type I and one type II AGN; one type I AGN and one SF components (we call all the three kinds as ‘type I’); two type II AGN (‘2-type II’); two SF components (‘2-SF’); one type II AGN and one SF components (‘type II + SF’). In practice, the quality of the current SDSS spectra does not allow us to distinguish the two cases: 2 type I AGN and type I+type II AGN. We generally classify them as type I *pp*-AGNs. Galaxies with weak [O III] and $H\beta$ (i.e. the amplitudes

⁶In practice, we directly pick up those objects with broad emission lines as type I AGN as given by conditions (6) or (7).

of both are lower than 3 times the standard deviation of the local continuum), and those with $z > 0.39$ ($H\alpha$ and $[N\ II]$ do not lie within the SDSS spectral coverage) can not be classified by the BPT diagram, are noted as “unknown-type” (hereafter “unknown”). We list numbers of each type of objects found in the present paper in Figure 1. Figures 5 and 6 show examples of the five types with images and spectra (*pp*-galaxies and asym-NEL galaxies).

Finally, we separate sources with strong $[O\ III]$ wings given in Table 5. They show interesting properties, which can be used to test outflow models, however, detailed discussions on the $[O\ III]$ -winged *pp*-galaxies are beyond the scope of this paper.

2.5. Comparison with previous samples

The present paper provides much more objects than previous samples (the total is ~ 190 *pp*-AGNs from W09 and L10) and covers *all* the known *pp*-AGNs from SDSS galaxy sample (DR7). The main reason for the dramatic increase of the number of objects is the selection criterion for AGN. The previous studies use the Kewley et al. (2001) criterion to select AGN in a more strict way whereas this work makes use of the empirical criterion by Kauffmann et al. (2003). We prefer this empirical criterion to classify the AGN and SF galaxies since sources located in the region between the Kauffmann and the Kewley et al. criteria are generally considered as AGN. In order to show the influence of the different criteria on the sizes of the resultant samples, we start from the 3,030 *pp*-galaxies selected by the present paper. Using the MPA measurements of the *pp*-galaxies, 222 *pp*-AGNs are left by applying the Kewley et al. criterion. Therefore, only 32 objects do not appear in the previous studies. These 32 objects are due to the $EW([O\ III])$ selection criterion: $EW([O\ III])$ is larger than 5\AA in W09, larger than 4\AA in L10, but larger than 3\AA in our work.

3. *pp*-galaxies: SDSS images

After selecting the two samples of *pp*-galaxies and asym-NEL galaxies, we visually inspect the SDSS images of the present samples (15,612 galaxies) to find dual-cored galaxies. Sub-structures of spiral galaxies could be regarded as dual-cored galaxies, but in practice it turns out that there are only a few of such cases in the present sample. The proper identification of substructures will require observing the spectrum of the second core in the future. If the dual-cored galaxies are due to projection effects (i.e. background or foreground galaxies), these pseudo dual-cored galaxies can be excluded if the redshift differences of the absorption lines is larger than 0.0017 (e.g. Patton et al. 2000). Visual inspection of potential dual-cores is limited by the SDSS image resolution ($\sim 1.4''$). We find 54 dual-cored *pp*-galaxies and asym-NEL galaxies from SDSS images, which are listed in Table 6 and Figure 11 of Appendix B. Among these galaxies, there are 14 2-type II AGN, 8 2-SF galaxies, 12 type II+SF galaxies, and 20 unknown-type galaxies (or noted by “unknown”). The 54 galaxies are the largest sample of dual-cored galaxies with double-peaked profiles from SDSS as far

as we know.

We stress here that the 54 dual-cored *pp*-galaxies and asym-NEL galaxies do not fully rule out the potential roles of the co-existing outflows. The observed double-peaked components could be contributed by the outflows such as Mrk 78 (Fisher et al. 2011). However, the current data does not allow us to separate the potential contributions of outflows. High quality observations of each cores should be made for more details of the dual-cored *pp*-galaxies. On the other hand, IFU observations are necessary to study the details of dynamics of merging galaxies.

Besides the 54 dual-cored *pp*-galaxies, visual inspection yields a by-product sample of 261 dual-cored *pp*-galaxies and asym-NEL galaxies, for which the second cores are beyond the SDSS 3'' fibers. We also check if the second cores have been observed by SDSS spectroscopic observation, and find 45 second cores with SDSS spectra. If the redshift difference between the primary and second cores is $\Delta z > 0.0017$, they could be irrelevant (Patton et al. 2000; Rogers et al. 2009; Lin et al. 2010). We exclude 6 of this kind of sources as foreground or background galaxies, or stars. The left 255 dual-cored galaxies in our samples are listed in Table 7 and Figure 12 of Appendix C. We find that there are two interesting *pp*-galaxies of which the second cores have asymmetric profiles. They are SDSS J001139.74-002827.8 accompanied by J001139.98-002826.1 (asym-NEL) and SDSS J115610.40+045935.0 by J115610.77+045943.4 (asym-NEL). Further observations (e.g. IFU) are needed to identify the origin of the emission-line profiles and the dynamics of the merging system.

We have checked FIRST radio images of the present *pp*-galaxies sample. It turns out that they show very interesting morphologies with different sizes. The results will be carried out in the second paper of this series. Though VLBA images of 87 *pp*-AGNs do not show evidence for dual cores (Tingay & Wayth 2011), a systematical VLBA survey is necessary among the present sample of the *pp*-galaxies.

4. Properties of *pp*-galaxies and asym-NEL galaxies

With the measurements of profile parameters, we can investigate correlations among them to explore the nature of the double peaks. However, we focus on the basic properties of the two samples of double-peaked narrow lines in this paper.

4.1. Redshift distributions

Figure 7*a,b* show the redshift distributions of different kinds of *pp*-galaxies and asym-NEL galaxies. The samples have a redshift range from 0 to 0.6, but 99% of the sources have $z < 0.3$. No significant differences among sub-samples have been found, implying the sub-samples are homogeneous in redshifts. There are no significant difference between *pp*-galaxies and asym-NEL galaxies. Figure 7*c* shows the redshift distribution of the 54 dual-cored *pp*-galaxies. They are

homogeneously distributed between $0.04 \leq z \leq 0.2$ with a mean value of $\langle z \rangle = 0.12$.

It should be mentioned that dual-cored galaxies (~ 310) found by Galaxy Zoo project (Darg et al. 2010, however they have not published their catalog so far.) are selected from $0.005 \leq z \leq 0.1$ galaxy sample of SDSS DR6. This image-selected sample of dual-cored galaxies is seriously suffering from the SDSS spatial resolution ($\Delta\theta \sim 1.4''$). The present sample is based on spectral profiles, and may cover some dual-cored candidates with more closer distance than Darg et al. sample, but should be identified through images with higher resolution. For example, NIR imaging observations with higher angular resolution are useful for identifying those galaxies with closer two cores (e.g. Fu et al. 2011, Shen et al. 2011, and Rosario et al. 2011). From Figure 7c, it is found that the dual-cored galaxies are not special populations in z -distributions.

4.2. ΔV distributions

After the host galaxy redshift is determined, the relative shifts of the blue and red peaks ($\Delta\lambda_b$ and $\Delta\lambda_r$) of pp -galaxies at [O III] wavelength can be obtained. Here $\Delta\lambda_b = \lambda_b - \lambda_0$, $\Delta\lambda_r = \lambda_r - \lambda_0$, λ_b and λ_r are the wavelengths of blue and red components respectively, and λ_0 is the wavelength of [O III] $\lambda 5007$ in the rest frame. The distributions of blueshift and redshift velocities are shown in Figure 8 *top* panels ($a_1 - e_1$), where the averaged velocities are indicated. We find the following properties from the distributions: 1) $\langle\Delta V_r\rangle$ is slightly larger than $\langle\Delta V_b\rangle$ by $\sim 60\text{km s}^{-1}$ for type I AGN whereas $\langle\Delta V_r\rangle$ and $\langle\Delta V_b\rangle$ have similar distributions in the other four types of pp -galaxies; 2) the shift ratio $\langle\log v\rangle = \langle\log |\Delta V_r/\Delta V_b|\rangle \simeq 0$ except for type I pp -AGNs; 3) 2-SF pp -galaxies generally have quite narrow distributions of redshifts and blueshifts whereas type I pp -AGN have relatively broad distributions.

$\Delta V_{r,b}$ distributions of the asym-NEL galaxies are shown in Figure 8 *bottom* panels ($a_2 - e_2$). From the five panels, we find: 1) $\langle\Delta V_r\rangle \sim \langle\Delta V_b\rangle$; 2) the shift ratio $\langle\log v\rangle \simeq 0$ for all the five kinds of galaxies; 3) the distribution properties are similar to pp -galaxies except for smaller velocity separations.

4.3. Distribution of flux ratios

Distributions of two integrated flux ratios of H α are shown in Figure 9a, and that of [O III] in Figure 9b. We find that the sample mainly distributes within [0.1, 10], which is a selecting bias. If flux ratios are too small or too large, the component with larger flux is dominating, and another component is so weak that it requires to be identified by higher S/N observations.

From Figure 9a, $F_{\text{H}\alpha}^r/F_{\text{H}\alpha}^b$ generally has narrow log-normal distributions for both pp -galaxies and asym-NEL galaxies. Except for type 1 pp -AGNs with broader $F_{\text{H}\alpha}^r/F_{\text{H}\alpha}^b$ distribution, the other types are very similar. Figure 9b shows $F_{[\text{O III}]}^r/F_{[\text{O III}]}^b$ distributions, similar to that of $F_{\text{H}\alpha}^r/F_{\text{H}\alpha}^b$,

but the former is relatively broader than the later. It is interesting to note that both $F_{\text{H}\alpha}^{\text{r}}/F_{\text{H}\alpha}^{\text{b}}$ and $F_{[\text{O III}]}^{\text{r}}/F_{[\text{O III}]}^{\text{b}}$ distributions in 2-SF are the narrowest among the five kinds of *pp*-galaxies and asym-NEL galaxies. This implies that there are undergoing processes with symmetric emission in 2-SF galaxies, that is to say, they could have either symmetric bi-polar outflows or circular rotation-supported NLR, or equal mass dual-cores. Finally, we find that the distributions of the flux ratios in *pp*-galaxies and asym-NEL galaxies are similar.

5. Conclusions

We have developed a pipeline to automatically select candidates of double-peaked galaxies of spectra. Combining with visual inspection of spectra, we set up the largest sample of double-peaked galaxies to date, which is composed of double-peaked narrow emission-line galaxies (3,030). We also build a sample of galaxies (12,582) with asymmetric and top-flat profiles from the SDSS DR7 galaxy sample. The *pp*-galaxies and the asym-NEL galaxies show very similar statistical properties, but velocity separations are significantly different. We find that double-peaked components are divided into 5 kinds, namely, type I *pp*-AGNs, 2-type II *pp*-AGNs, (AGN+SF) *pp*-galaxies, 2-SF and unknown-type objects depending on the Balmer line width and the Baldwin-Phillips-Terlevich diagram. The *pp*-galaxies sample covers: 81 type I *pp*-AGNs, 837 2-type II *pp*-AGNs, 400 type II+SF *pp*-galaxies, 708 2-SF and 1,004 unknown-type objects. We visually inspect the SDSS images of the sample and find 54 galaxies with dual-cores, of which 14 2-type II *pp*-AGNs, 8 2-SF, 12 type II+SF *pp*-galaxies and 20 unknown-type objects.

We would draw the following conclusions in light of the present sample:

- The fractions of *pp*-galaxies and asym-NEL galaxies to emission-line galaxies are about 1.0% and 3.6%, respectively, and *pp*-AGNs (including type I, 2-type II, type II +SF *pp*-galaxies) and asym-NEL AGN are about 0.4% and 1.5%, respectively.
- From the two samples, we find 54 dual cored galaxies with projected separation smaller than 3'' and 255 with that larger than 3''. Observations with higher spatial resolution or in X-ray or radio bands are needed to identify dual-cores from images of rest objects of the present samples, in particular, the sub-samples of type I and AGN+SF *pp*-galaxies.

Future observations with for example the *LAMOST/Guoshoujing* (a 4-m telescope with 4,000 fibers) through images and spectra of the two components are needed to understand the nature of the *pp*-galaxies. The large sample can be used to study the dynamical processes of merging galaxies, the triggering mechanisms of AGN activity, outflows and rotation-supported disk of narrow line regions.

We are very grateful to the anonymous referee for a large number of helpful comments and suggestions in careful reports, which improved the manuscript. JMW thanks David Valls-Gaubald

for carefully reading the manuscript and suggestions. We appreciate the stimulating discussions among the members of IHEP AGN group, especially, Long Di, Han-Qin Gao and Zhen Zhang, who visually re-checked the images of 15,000 double-peaked galaxies, and Yan-Rong Li for useful discussions on star formation driven by tidal interaction. The research is supported by NSFC-10733010, 10821061, 10903008 and 11133006, and 973 project (2009CB824800). SZ thanks support of NSFC-11073021 and 11133002. Funding for the SDSS and SDSS-II has been provided by the Alfred P. Sloan Foundation, the Participating Institutions, the National Science Foundation, the U.S. Department of Energy, the National Aeronautics and Space Administration, the Japanese Monbukagakusho, the Max Planck Society, and the Higher Education Funding Council for England. The SDSS Web Site is <http://www.sdss.org/>. The SDSS is managed by the Astrophysical Research Consortium for the Participating Institutions. The Participating Institutions are the American Museum of Natural History, Astrophysical Institute Potsdam, University of Basel, University of Cambridge, Case Western Reserve University, University of Chicago, Drexel University, Fermilab, the Institute for Advanced Study, the Japan Participation Group, Johns Hopkins University, the Joint Institute for Nuclear Astrophysics, the Kavli Institute for Particle Astrophysics and Cosmology, the Korean Scientist Group, the Chinese Academy of Sciences (LAMOST), Los Alamos National Laboratory, the Max-Planck-Institute for Astronomy (MPIA), the Max-Planck-Institute for Astrophysics (MPA), New Mexico State University, Ohio State University, University of Pittsburgh, University of Portsmouth, Princeton University, the United States Naval Observatory, and the University of Washington.

REFERENCES

- Abazajian, K. N., et al. 2009, *ApJS*, 182, 543
- Baldwin, J. A., Phillips, M. M. & Terlevich, R. 1981, *PASP*, 93, 5
- Barrows, R. S. et al. 2012, *ApJ*, 744, 7
- Bennert, N. et al. 2002, *ApJ*, 574, L105
- Bennert, N. et al. 2006a, *A&A*, 456, 953
- Bennert, N. et al. 2006b, *A&A*, 459, 55
- Bernardi, M. et al. 2003, *AJ*, 125, 1817
- Bicknell, G. et al. 1998, *ApJ*, 495, 680
- Bruzual, G. & Charlot, S. 2003, *MNRAS*, 344, 1000
- Capetti, A. et al. 1999, *ApJ*, 516, 187
- Cardelli, J. A., Clayton, G. C. & Mathis, J. S., 1989, *ApJ*, 345, 245

- Cid Fernandes, R. et al. 2005, MNRAS, 358, 363
- Comerford, J. M. et al. 2009a, ApJ, 698, 956
- Comerford, J. M. et al. 2009b, ApJ, 702, L82
- Comerford, J. M., Gerke, B. F., Stern, D., et al. 2012, ApJ, 753, 42
- Crenshaw, D. M. & Kraemer, S. B. 2000, ApJ, 532, L101
- Crenshaw, D. M. et al. 2000, AJ, 120, 1731
- Crenshaw, D. M., Kraemer, S. B., Schmitt, H. R. et al. 2010a, AJ, 139, 871
- Crenshaw, D. M., Schmitt, H. R., Kraemer, S. B. et al. 2010b, ApJ, 708, 419
- Darg, D. W. et al. 2010, MNRAS, 401, 1552
- Das, V., et al. 2005, AJ, 130, 945
- Das, V., Crenshaw, D. M., Kraemer, S. B., & Deo, R. P. 2006, AJ, 132, 620
- Das, V., Crenshaw, D. M., & Kraemer, S. B. 2007, ApJ, 656, 699
- Dumas, G, et al. 2007, MNRAS, 379, 1249
- Eracleous, M. et al. 2011, arXiv: 1106.2952
- Fisher, T. C., Crenshaw, D. M., Kraemer, S. B. et al. 2010, AJ, 140, 577
- Fisher, T. C., Crenshaw, D. M., Kraemer, S. B. et al. 2011, ApJ, 727, 71
- Fu, H. et al. 2011, ApJ, 733, 103
- Fu, H. et al. 2012, ApJ, 745, 67
- Gerke, B. F. et al. 2007, ApJ, 660, 23
- Greene, J. E. & Ho, L. C. 2005, ApJ, 627, 721
- Greene, J. E., & Ho, L. C. 2006, ApJ, 641,117
- Hao, L., Strauss, M. A., Tremonti, C. A., et al. 2005, AJ, 129, 1783
- Heckman, T. M. et al. 1981, ApJ, 247, 403
- Heckman, T. M. et al. 1984, ApJ, 281, 525
- Ho, L. C. 2009, ApJ, 699, 638
- Ho, L. C. et al, 2009, ApJS, 183, 1

- Hutchings, J. B. et al. 1998, *ApJ*, 492, L115
- Kauffmann, G. et al. 2003, *MNRAS*, 346, 1055
- Keel, W. C. 1985, *Nature*, 318, 43
- Kewley, L. J. et al. 2001, *ApJ*, 556, 121
- Lagos, C. D. P. et al. 2011, *MNRAS*, 414, 2148
- Lin, L.-H. et al. 2010, *ApJ*, 718, 1158
- Liu, X. et al. 2010a, *ApJ*, 708, 427
- Liu, X. et al. 2010b, *ApJ*, 715, L30
- Longair, M. 2008, *Galaxy formation*, Berlin: Springer
- Lupton, R. H. 1993, *Statistics in Theory and Practice* (Princeton: Princeton Univ. Press)
- McGurk, R. C. et al. 2011, *ApJ*, 738, L2
- Osterbrock, D. E., & Ferland, G. J. (ed.) 2006, *Astrophysics of Gaseous Nebulae and Active Galactic Nuclei* (Sausalito, CA: Univ. Science Books)
- Patton, D. R. et al. 2000, *ApJ*, 536, 153.
- Peng, Z., Chen, Y.-M., Gu, Q.-S. & Hu, C. 2011, *RAA*, 11, 411
- Rogers, B. et al. 2009, *MNRAS*, 399, 2172
- Rosario, D. J. et al. 2008, *MmSAI*, 79, 1217
- Rosario, D. J. et al. 2010, *ApJ*, 716, 131
- Rosario, D. J. et al. 2011, *ApJ*, 739, 44
- Ruiz, J. R., Crenshaw, D. M., Kraemer, S. B., Bower, G. A., Gull, T. R. et al. 2001, *AJ*, 122, 2961
- Schlesinger, K., Pogge, R. W., Martini, P., Shields, J. C., & Fields, D. 2009, *ApJ*, 699, 857
- Shen, S. Y. et al. 2010, *ApJ*, 725, L210
- Shen, Y. et al. 2011, *ApJ*, 735, 48
- Smith, K., L. et al. 2010, *ApJ*, 716, 866
- Schmitt, H. R. et al. 2003, *ApJS*, 148, 327
- Steffen, W. et al. 1997, *MNRAS*, 286, 1032

- Stoklasová, I. et al. 2009, *A&A*, 500, 1287
- Tingay, S. J. & Wayth, R. B. 2011, *AJ*, 141, 174
- Tsalmantza, P. et al. 2011, *ApJ*, 738, 20
- Vega Beltrán, J. C. et al. 2001, *A&A*, 374, 394
- Valdes, F. et al. 2004, *ApJS*, 152, 251
- Wang, J.-F., Fabbiano, G. et al. 2011, *ApJ*, 736, 62
- Wang, J.-M., Chen, Y.-M. et al. 2009, *ApJ*, 705, L76
- Whittle, M. 1985a, *MNRAS*, 213, 1
- Whittle, M. 1985b, *MNRAS*, 213, 33
- Whittle, M. 1985c, *MNRAS*, 216, 817
- Whittle, M. 1992, *ApJ*, 387, 121
- Whittle, M. & Wilson, A. S. 2004, *AJ*, 127, 606
- Wilson, A. S. & Willis, A. G. 1980, *ApJ*, 240, 429
- Xu, D. & Komossa, S. 2009, *ApJ*, 705, L20
- Yu, Q. et al. 2011, *ApJ*, 738, 92
- Zhou, H. et al. 2004, *ApJ*, 604, L33

Table 1. Summary of SDSS samples of double-peaked AGN

Sample	Selection methods	Object number	Notes
W09	$r < 17.7, z \leq 0.15, EW([O III]) > 5\text{\AA}, 0.1 \leq F_{\text{red}}/F_{\text{blue}} \leq 10$	87	only type II AGN
L10	$S/N > 5, [O III] > 5\sigma, EW([O III]) \geq 4\text{\AA}, [O III]/H\beta > 3$	146+21	only type II AGN+QSO
S10	$0.1 \leq z \leq 0.7$ QSOs	148	type I, II
Others	individual objects	8	<i>pp</i> -AGNs
This work	see Figure 1	3,030+12,582	covers all previous galaxies
<i>pp</i> -AGNs observed with near infrared (NIR) higher spatial resolution, long slit spectroscopy and Integral Field Unit (IFU)			
Fu11	from W09+L10+Smith10; NIR image	17+33	mergers: 8/17+8/33
Shen11	from L10; NIR image+long slit spectroscopy	31	mergers: 5
R11	from Smith10; NIR image	12	mergers: 6
Fu12	from W09+L10+Smith10; IFU	42	dual AGN: 2
C11	from W09+L10; long slit spectroscopy	81	dual AGN candidates: 17

Note. — References: C11: Comerford et al. (2011); Fu11: Fu et al. (2011); Fu12: Fu et al. (2012); L10: Liu et al. (2010a); R11: Rosario et al. (2011); S10: Smith et al. (2010); Shen11: Shen et al. (2011); W09: Wang et al. (2009);
 — Others: SDSS J09527.62+255257.2 (McGurk et al. 2011), COSMOS J100043.15+020637.2 (Comerford et al. 2009b), SDSS J104807.74+005543.5 (Zhou et al. 2004), SDSS J131642.90+175332.5 (Xu & Komossa 2009), EGSD2 J141550.8+520929 (Comerford et al. 2009a), EGSD2 J142033.66+525917.5 (Gerke et al. 2007), SDSS J142507.32+323137.4 (Peng et al. 2011), CXOXB142607.6+353351 (Barrows et al. 2012).
 — In Fu11, 17 type I AGN and 33 type II AGN are imaged by Keck II LGSAO in the NIR, in which 8 type I AGN and 8 type II AGN are found to be mergers.
 — 3,030 *pp*-galaxies and 12,582 asym-NEL galaxies are found in this work.
 — We would like to stress the different criterion to select *pp*-AGNs in W09 and L10 from the present paper. The Kauffmann et al. (2003) criterion (empirical one) is used in the present paper whereas the Kewley et al. (2001) criterion was used in W09 and L10.

Table 2. Eight fitting models of different groups of emission lines

model\group	narrow Gaussian	narrow Gaussian	[O III] wing	broad Balmer
M1	✓			
M2	✓	✓		
M3	✓		✓	
M4	✓			✓
M5	✓		✓	✓
M6	✓	✓		✓
M7	✓	✓	✓	
M8	✓	✓	✓	✓

Note. — M1-M8 are the eight fitting models which are different combinations of four emission-line groups: two narrow Gaussian groups, one [O III] wing group, and one broad Balmer group.

Table 3. Emission-line galaxies with double-peaked NELs

SDSS name (1)	mjd (2)	plate (3)	fiber (4)	z (5)	r (6)	σ_* (7)	ΔV_b (8)	ΔV_r (9)	σ_b (10)	σ_r (11)	$F_{[\text{OIII}]}$ ^b (12)	$F_{[\text{OIII}]}$ ^r (13)	$F_{\text{H}\alpha}$ ^b (14)	$F_{\text{H}\alpha}$ ^r (15)	Type (16)
type I															
J011935.64-102613.2	52163	661	285	0.12479± 0.00004	17.32	138± 10	-76± 8	235± 4	161± 5	125± 2	764± 38	831± 37	343± 9	250± 9	1
J040001.59-065254.1	51908	464	104	0.17003± 0.00003	16.87	227± 7	-144± 6	229± 3	183± 5	142± 2	734± 30	813± 29	243± 7	288± 8	1
J074156.55+294135.6	52663	889	271	0.12115± 0.00003	16.77	119± 8	-110± 5	103± 5	92± 4	77± 3	28± 2	18± 2	178± 12	135± 12	1
J075017.49+270304.1	52316	858	437	0.14104± 0.00003	16.84	150± 9	-90± 9	133± 8	111± 5	94± 4	52± 4	21± 3	307± 16	234± 21	1
2-type II															
J000249.07+004504.8	51793	388	345	0.08650± 0.00004	16.08	221± 12	-248± 3	238± 2	162± 3	158± 2	444± 12	639± 21	446± 15	551± 15	2
J000656.85+154847.9	52251	751	504	0.12498± 0.00002	16.92	152± 6	-193± 7	174± 6	156± 4	151± 4	493± 22	502± 22	188± 6	225± 6	2
J001630.41-003801.6	51795	389	163	0.06346± 0.00003	16.20	169± 8	-135± 4	176± 4	125± 3	119± 3	59± 3	38± 2	516± 21	524± 26	2
J002202.11-100744.1	52145	653	227	0.24761± 0.00006	17.70	254± 15	-283± 19	131± 22	136± 15	205± 20	27± 4	41± 4	9± 4	48± 5	2
type II+SF															
J000712.22+155207.9	52251	751	578	0.16131± 0.00005	17.52	230± 15	-154± 12	186± 14	113± 11	135± 12	3± 1	4± 1	80± 28	94± 27	3
J001050.52-103246.8	52141	651	108	0.15711± 0.00021	17.41	396± 56	-316± 2	-44± 8	77± 4	204± 6	33± 3	87± 3	128± 11	423± 19	3
J002418.69-003426.1	53734	1542	63	0.34060± 0.00016	19.00	190± 43	-40± 7	218± 2	151± 5	87± 2	57± 2	33± 2	210± 6	156± 5	3
J005104.37+152101.2	51871	420	436	0.15528± 0.00005	17.82	180± 15	-125± 4	171± 8	99± 3	114± 6	10± 0	13± 1	165± 12	116± 15	3
2-SF															
J000511.71+153846.2	52251	751	427	0.05356± 0.00003	15.16	182± 7	-110± 5	183± 6	127± 3	108± 4	30± 1	21± 2	713± 36	450± 35	4
J000728.10-003617.1	52559	669	93	0.32712± 0.00008	19.07	135± 23	-123± 13	127± 12	95± 12	79± 10	0± 0	0± 0	30± 15	24± 11	4
J001139.74-002827.8	52913	1089	205	0.05699± 0.00003	0.00	93± 8	9± 1	429± 3	91± 1	93± 3	18± 1	33± 2	403± 24	80± 6	4
J002010.68-004852.8	51900	390	226	0.14129± 0.00002	16.07	181± 6	-118± 7	127± 7	94± 6	91± 5	3± 0	4± 0	73± 14	69± 11	4
unknown-type															
J000218.20-110139.5	52143	650	81	0.11959± 0.00002	16.76	172± 6	-118± 9	125± 14	79± 8	113± 12	12± 3	16± 3	72± 14	86± 13	5
J000503.84+010629.6	52559	669	364	0.23857± 0.00007	18.79	151± 20	-86± 19	199± 9	122± 15	103± 7	2± 0	2± 0	43± 8	64± 9	5
J001552.74-085430.9	52138	652	409	0.13692± 0.00008	17.39	281± 22	-181± 17	239± 9	216± 16	116± 8	5± 0	12± 2	132± 25	75± 16	5
J001746.35-005052.7	52518	687	45	0.19020± 0.00004	17.82	170± 11	-123± 15	150± 16	88± 12	103± 17	1± 0	3± 1	28± 10	28± 9	5

Note. — Table 3 is available in its entirety via the link to the machine-readable version above.

Column 1: SDSS DR7 designation hmmm.ss+ddmmss.s (J2000.0). Column 2: MJD of spectroscopic observation. Column 3: Plate of spectroscopic observation. Column 4: Fiber of spectroscopic observation. Column 5: Redshift of spectroscopic observation. Column 6: Magnitude in r -band. Column 7: Velocity dispersion of galaxy absorption lines in units of km/s. Column 8 and 9: the Doppler blueshifts and redshifts of the blue and red components of NELs in units of km/s, respectively. Column 10 and 11 are the corresponding velocity dispersion in units of km/s. Column 12 and 13 are the corresponding [O III] flux in units of $10^{-17} \text{erg s}^{-1} \text{cm}^{-2}$. Column 14 and 15 are the corresponding H α flux in units of $10^{-17} \text{erg s}^{-1} \text{cm}^{-2}$. Column 16: The type of the pp -galaxy: 1 standards for type I, 2 for 2-type II, 3 for type II + SF, 4 for 2-SF, and 5 for 'unknown-type'.

– The machine-readable version of this table gives more effective numbers from Column (7) to (15).

Table 4. Emission-line galaxies with asymmetric and top-flat NELs

SDSS name (1)	mjd (2)	plate (3)	fiber (4)	z (5)	r (6)	σ_* (7)	ΔV_b (8)	ΔV_r (9)	σ_b (10)	σ_r (11)	$F_{[\text{OIII}]}$ ^b (12)	$F_{[\text{OIII}]}$ ^r (13)	$F_{\text{H}\alpha}$ ^b (14)	$F_{\text{H}\alpha}$ ^r (15)	Type (16)
type I															
J011935.64-102613.2	52163	661	285	0.12479± 0.00004	17.32	139± 11	-77± 8	235± 5	161± 5	125± 3	765± 39	832± 37	344± 9	250± 9	1
J040001.59-065254.1	51908	464	104	0.17003± 0.00003	16.87	227± 8	-144± 7	229± 4	183± 5	143± 3	735± 30	814± 30	243± 8	288± 9	1
J074156.55+294135.6	52663	889	271	0.12115± 0.00003	16.77	120± 8	-111± 6	103± 6	92± 4	78± 4	29± 2	19± 2	178± 12	136± 12	1
J075017.49+270304.1	52316	858	437	0.14104± 0.00003	16.84	151± 10	-90± 9	133± 9	112± 5	95± 5	52± 4	22± 3	307± 17	235± 22	1
2-type II															
J000249.07+004504.8	51793	388	345	0.08650± 0.00004	16.08	222± 12	-248± 3	239± 3	163± 3	159± 3	444± 13	639± 22	447± 16	551± 16	2
J000656.85+154847.9	52251	751	504	0.12498± 0.00002	16.92	152± 6	-194± 8	174± 7	157± 5	152± 4	493± 22	502± 22	189± 6	226± 6	2
J001630.41-003801.6	51795	389	163	0.06346± 0.00003	16.20	170± 8	-135± 5	177± 5	126± 4	119± 3	59± 3	38± 3	517± 21	524± 26	2
J002202.11-100744.1	52145	653	227	0.24761± 0.00006	17.70	254± 16	-283± 19	132± 23	136± 16	206± 20	28± 5	41± 5	9± 4	49± 5	2
type II+SF															
J000712.22+155207.9	52251	751	578	0.16131± 0.00005	17.52	230± 15	-155± 12	187± 15	114± 11	136± 13	4± 2	4± 1	81± 29	94± 27	3
J001050.52-103246.8	52141	651	108	0.15711± 0.00021	17.41	396± 56	-316± 3	-45± 8	77± 4	205± 6	33± 4	87± 4	128± 11	423± 19	3
J002418.69-003426.1	53734	1542	63	0.34060± 0.00016	19.00	190± 44	-41± 8	218± 3	152± 5	87± 3	58± 2	33± 2	211± 6	157± 6	3
J005104.37+152101.2	51871	420	436	0.15528± 0.00005	17.82	180± 15	-125± 4	172± 8	99± 4	115± 7	11± 1	13± 2	165± 13	117± 16	3
2-SF															
J000511.71+153846.2	52251	751	427	0.05356± 0.00003	15.16	182± 7	-111± 5	183± 6	127± 4	109± 4	30± 2	21± 2	714± 36	450± 36	4
J000728.10-003617.1	52559	669	93	0.32712± 0.00008	19.07	135± 24	-123± 13	128± 12	96± 13	79± 11	1± 0	1± 0	30± 15	24± 11	4
J001139.74-002827.8	52913	1089	205	0.05699± 0.00003	0.00	94± 8	9± 1	430± 4	91± 1	93± 4	19± 1	34± 3	404± 24	81± 7	4
J002010.68-004852.8	51900	390	226	0.14129± 0.00002	16.07	182± 7	-118± 8	127± 8	94± 6	92± 6	4± 1	5± 1	73± 14	69± 12	4
unknown-type															
J000218.20-110139.5	52143	650	81	0.11959± 0.00002	16.76	172± 7	-119± 10	125± 15	80± 8	114± 12	13± 3	16± 3	73± 15	87± 14	5
J000503.84+010629.6	52559	669	364	0.23857± 0.00007	18.79	152± 21	-86± 19	199± 10	123± 15	104± 7	3± 1	3± 1	43± 9	65± 9	5
J001552.74-085430.9	52138	652	409	0.13692± 0.00008	17.39	282± 22	-181± 18	239± 9	217± 16	117± 9	5± 1	13± 3	132± 26	76± 16	5
J001746.35-005052.7	52518	687	45	0.19020± 0.00004	17.82	170± 11	-124± 15	151± 17	88± 13	103± 17	2± 1	3± 1	29± 10	28± 9	5

Note. — Table 4 is available in its entirety via the link to the machine-readable version above.
See note in Table 3.

Table 5. List of *pp*-AGN (110) and asym-NEL AGN (235) with strong [O III] wings

No. (1)	SDSS name (2)	mjd (3)	plate (4)	fiber (5)	z (6)	r (7)	$\Delta V_{[\text{OIII}] \text{wing}}$ (8)	$\log L_{[\text{OIII}] \text{wing}}$ (9)	type (10)
1	J011935.64–102613.2	52163	661	285	0.124940	17.32	80.3	41.69	type I <i>pp</i> -AGN
2	J040001.59–065254.1	51908	464	104	0.170160	16.87	132.2	41.96	type I <i>pp</i> -AGN
3	J080329.02+532233.5	53384	1871	290	0.219440	17.79	181.4	41.35	type I <i>pp</i> -AGN
4	J081203.34+571356.7	53386	1872	416	0.087510	15.67	-112.5	41.61	type I <i>pp</i> -AGN
5	J082256.27+332201.4	52325	862	495	0.138940	17.28	-67.2	41.28	type I <i>pp</i> -AGN
6	J084634.20+312944.8	52991	1270	438	0.120960	16.80	-138.5	40.84	type I <i>pp</i> -AGN
7	J085944.13+295408.4	53357	1934	365	0.048770	15.43	-82.3	39.91	type I <i>pp</i> -AGN
8	J091544.19+300922.0	53379	1938	309	0.129380	16.47	259.2	41.88	type I <i>pp</i> -AGN
9	J093549.73+072502.2	52733	1196	106	0.213880	17.14	-86.8	41.18	type I <i>pp</i> -AGN
10	J095950.32–001339.0	51633	268	146	0.090670	16.83	-41.0	41.31	type I <i>pp</i> -AGN
...

Note. — Table 5 is available in its entirety via the link to the machine-readable version above. Columns (1)-(7) are No., SDSS name, mjd, plate, fiber, redshifts and r -band magnitude, respectively. Column (8) is shift of the strong wings in km s^{-1} , and (9) is the luminosity in erg s^{-1} . Column (10) indicates the types of the objects.

Table 6. List of 54 dual-cored *pp*-galaxies and asym-NEL galaxies

No.	SDSS name	mjd	plate	fiber	<i>z</i>	<i>r</i>	type
1	J030558.72–005027.5	52289	802	71	0.154710	19.13	2-type II
2	J075055.44+354411.4	52017	543	224	0.135580	17.10	unknown
3	J103618.74+152310.1	54177	2594	244	0.065870	15.80	unknown
4	J103801.87+371643.2	53432	1973	625	0.119080	16.22	2-type II
5	J111834.31+294110.7	53793	2215	543	0.138940	18.11	type II+SF
6	J112555.93+142206.4	53385	1754	317	0.208830	18.78	type II+SF
7	J121900.51+152442.2	53436	1767	344	0.241500	17.72	2-SF
8	J122222.25+022038.6	52282	518	28	0.111020	16.40	unknown
9	J122239.58+134638.5	53436	1767	218	0.080020	16.71	unknown
10	J130242.81+143405.4	53498	1771	111	0.142160	16.91	unknown
11	J135224.16+181144.3	54508	2756	262	0.168460	16.71	unknown
12	J143615.95+560124.1	52668	1162	448	0.140700	17.49	unknown
13	J144420.56+120742.9	53531	1712	158	0.029140	15.44	unknown
14	J145059.71–000215.2	51994	309	304	0.043080	13.85	unknown
15	J164648.33+262857.4	53260	1691	311	0.137350	16.76	2-type II
16	J002856.80+004037.7	51782	391	534	0.090060	16.68	type II+SF
17	J021242.27+002903.8	53763	1507	421	0.150020	17.48	type II+SF
18	J034508.79–005546.6	54465	2639	44	0.226760	18.22	unknown
19	J080030.74+440720.4	51876	437	361	0.131870	16.60	2-SF
20	J081948.05+254329.0	52962	1585	450	0.082080	18.08	type II+SF
21	J094410.57+654744.8	54468	1788	442	0.138870	17.31	type II+SF
22	J100443.64+062555.0	52731	995	600	0.163760	19.17	2-type II
23	J102700.40+174901.0	54140	2591	480	0.066580	15.20	unknown
24	J102938.95+375030.0	53432	1973	405	0.151760	19.64	2-type II
25	J103846.97+155359.0	54177	2594	498	0.194230	17.82	type II+SF
26	J105045.75+664146.9	51929	490	430	0.098970	16.43	unknown
27	J111506.62+132913.0	53379	1752	54	0.169970	16.55	unknown
28	J112756.91+245934.1	54154	2497	593	0.115100	17.03	2-type II
29	J112850.25+190339.8	54180	2502	314	0.166330	17.82	2-SF
30	J114617.47+145305.2	53415	1762	263	0.173420	18.05	2-type II
31	J123656.65+254129.8	54498	2659	611	0.087220	16.06	2-type II
32	J124132.12+535257.3	52673	1038	298	0.083270	15.80	2-type II
33	J135046.61+315138.4	53503	2024	20	0.105600	17.33	unknown
34	J135313.15+475256.9	52736	1284	38	0.124390	16.61	unknown
35	J135830.04+182736.1	54509	2757	382	0.063010	15.88	type II+SF
36	J140247.81+144900.8	54272	2744	124	0.225760	16.74	unknown
37	J142032.07+020351.5	51994	533	35	0.068740	15.87	2-type II
38	J142606.65+202831.6	54552	2787	183	0.076810	16.12	type II+SF
39	J143246.31–020617.7	52409	919	275	0.056270	15.11	2-type II
40	J143520.64+185842.7	54535	2775	431	0.180770	17.41	2-type II
41	J145320.90+060626.0	54560	1830	426	0.093900	16.75	type II+SF
42	J145857.24+090232.4	53884	1815	377	0.137920	16.86	2-SF
43	J151109.24–015229.7	52404	923	238	0.124740	17.67	unknown
44	J151706.75+060645.7	54561	1833	545	0.044910	15.83	2-SF
45	J151713.62+331008.6	53116	1386	173	0.082200	16.05	2-type II
46	J154412.23+274955.6	53534	1653	154	0.116290	17.72	2-SF
47	J155708.82+273518.7	52822	1392	400	0.124170	16.27	unknown
48	J160102.81+070612.1	53858	1729	400	0.139390	17.61	type II+SF
49	J161037.33+073852.3	53498	1730	180	0.130230	17.43	type II+SF
50	J204631.42+001708.8	52466	982	416	0.137170	17.25	2-SF
51	J205708.39+010805.2	52442	984	369	0.060500	16.44	unknown
52	J220329.87+123327.6	52519	735	302	0.151040	17.62	2-type II
53	J220804.49+010805.8	51788	373	523	0.085490	15.56	unknown
54	J221924.98–093821.6	52203	719	7	0.094870	15.95	2-SF

Note. — The images and the spectra of the 54 galaxies are shown in Figure 11. The number sequence of the images should be from *left to right* and from *top to bottom*. No. 1-15 are *pp*-galaxies and 16-54 are asym-NEL galaxies.

Table 7. List of 255 galaxies with dual cores separated $\geq 3''$

No.	primary core						secondary core						Note
	SDSS name	mjd	plate	fiber	z	r	SDSS name	mjd	plate	fiber	z	r	
1	J090012.70+183439.2	53729	2283	160	0.08118	16.97	J090012.30+183436.8	53700	2285	316	0.08040	17.17	normal galaxy
2	J101455.13+003337.5	51909	270	586	0.18723	17.16							
3	J135432.27+582345.8	52668	1158	517	0.06061	14.34							
4	J000249.07+004504.8	51793	388	345	0.08663	16.08	J000249.44+004506.7	52203	685	593	0.08653	16.43	normal galaxy
5	J081423.00+033628.3	52641	1184	230	0.17077	19.28							
6	J081705.22+032146.2	52641	1184	53	0.09329	17.11							
7	J091954.54+325559.8	52990	1592	160	0.04928	17.43							
8	J095900.10+293337.6	53436	1950	218	0.17887	17.54							
9	J100602.14+071131.0	52751	1236	54	0.12148	18.62	J100602.51+071131.8	52641	996	328	0.12051	15.77	normal galaxy
10	J102207.37-000415.5	51883	271	39	0.12547	17.26							

- Note. — Table 7 is available in its entirety via the link to the machine-readable version above.
- It should be noted that SDSS fibers only cover $3''$ and the double-peaked profiles of these source *only* originate from *one* of the cores marked by red square in the images given by Figure 12 as shown by Appendix C.
 - There are 39 sources with SDSS spectra observation of the secondary core, and have $\Delta z < 0.0017$ (500 km/s). The last column shows the property of the secondary core: normal (single-peaked) galaxy, *pp*-galaxy, *asym*-NEL galaxy.

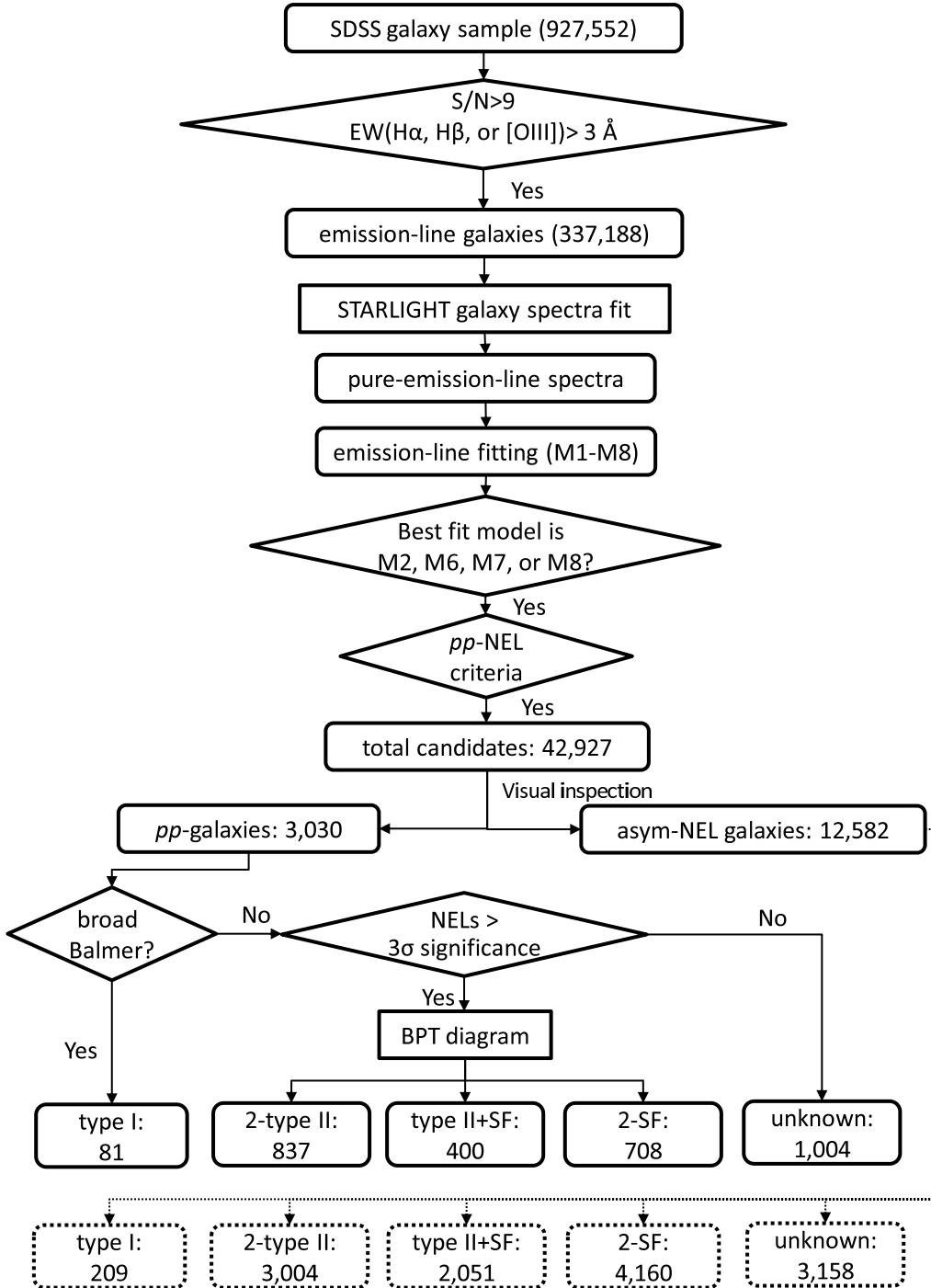


Fig. 1.— Flowchart of sample selection. M1-M8 are the eight models used for fitting the pure emission-line spectra. The dashed line shows that asym-NEL galaxies are also classified by the same method as double-peaked sources. The numbers indicated in squares are the amount of the corresponding objects.

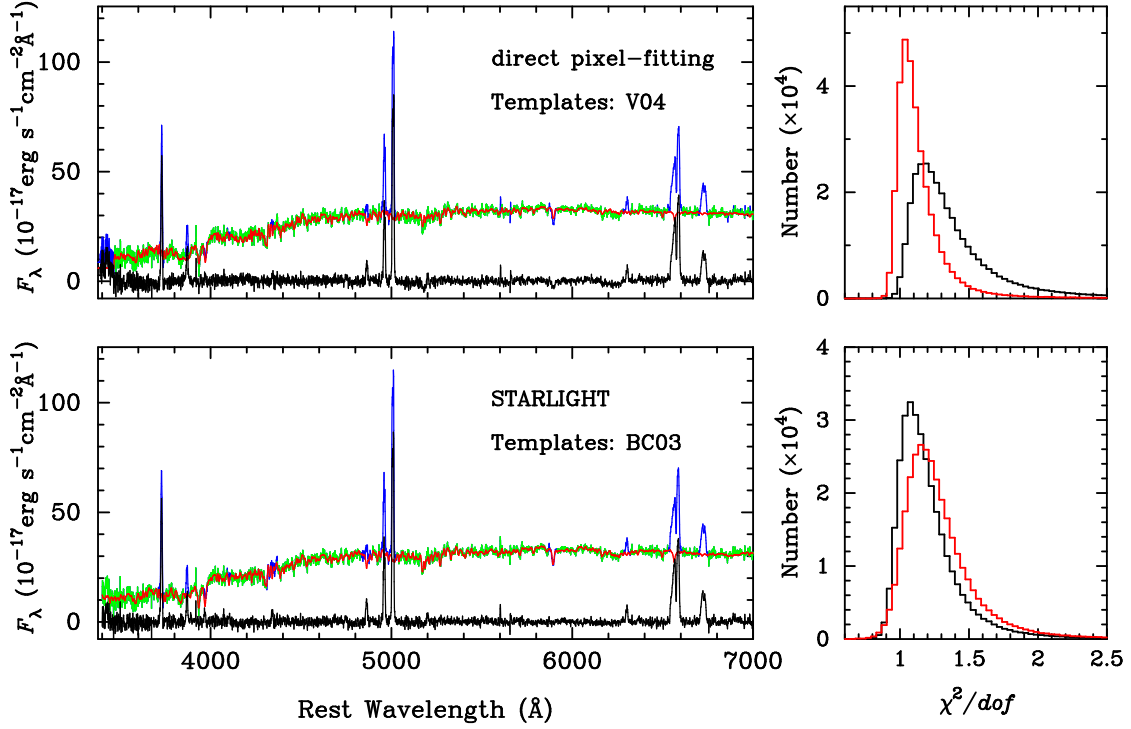


Fig. 2.— Example of galactic spectra (SDSS J000656.85+154847.9) fitting with stellar templates (V04, *top left*) by using the direct pixel-fitting method and with stellar population templates (BC03, *bottom left*) by using the STARLIGHT code. The green and blue lines are the observed spectra. During the absorption line fitting, the blue lines are masked to eliminate the influence of the emission lines and we only use the points labeled as green for fitting. The red lines are the fitted stellar spectra. The black lines represent the residual spectra. The corresponding χ^2 distributions of the fits with the direct pixel-fitting method (*top right*) and the STARLIGHT code (*bottom right*) are also shown. The black lines represent the χ^2 calculated from the total fitting range. The red lines represent the χ^2 calculated in the restricted region 3910-4060Å and 5250-5820Å of the total fitting range, which covers the Ca II H+K and Mg Ib triplet absorption lines.

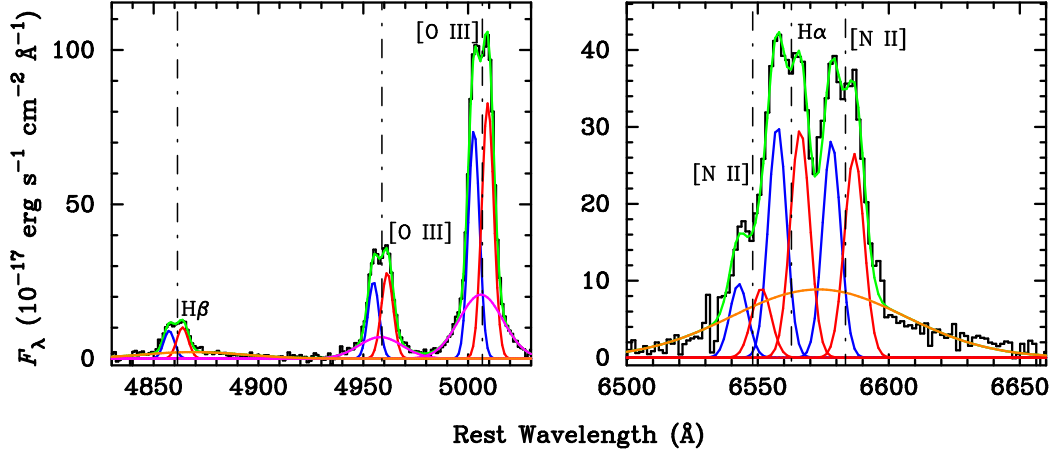


Fig. 3.— Example of a pure emission-line spectrum after subtracting the stellar contribution of its host galaxy. We fit the spectrum with different emission line components (SDSS J123605.45-014119.2). The black lines represent the pure emission-line spectrum, the blue lines show one narrow Gaussian group, and the red lines show another narrow Gaussian group, the pink line stands for the broader [O III] wings, while the brown lines represent the broad Balmer lines ($H\alpha$ and $H\beta$). The green lines shows the final fitting model.

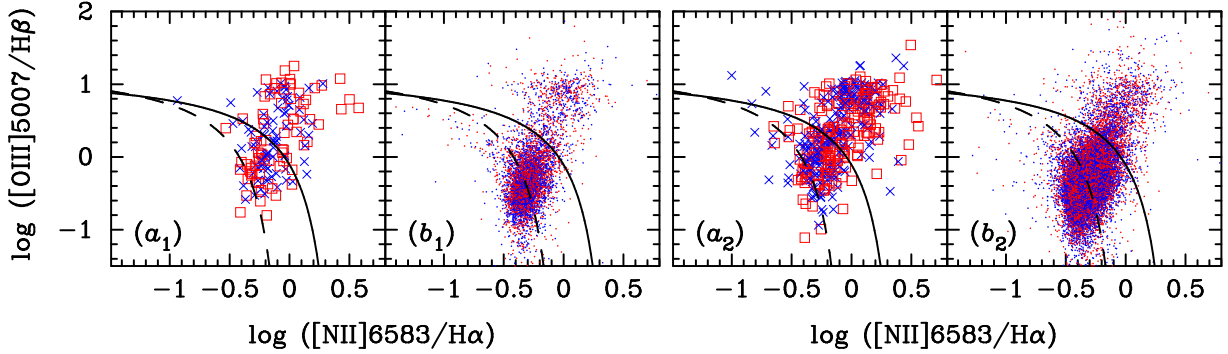


Fig. 4.— BPT diagrams of blue and red components of *pp*-galaxies (a_1, b_1) and asym-NEL galaxies (a_2, b_2). The solid and dashed lines correspond to the dividing lines between AGN and SF galaxies given by Kewley et al. (2001) and Kauffmann et al. (2003), respectively. The blue cross symbols in panel (a_1) and (a_2) correspond to the blue component and the red rectangles represent the red component of NELs of type I AGN. The blue and red points in panel (b_1) and (b_2) correspond to the blue and red components of the NELs of narrow-line galaxies respectively.

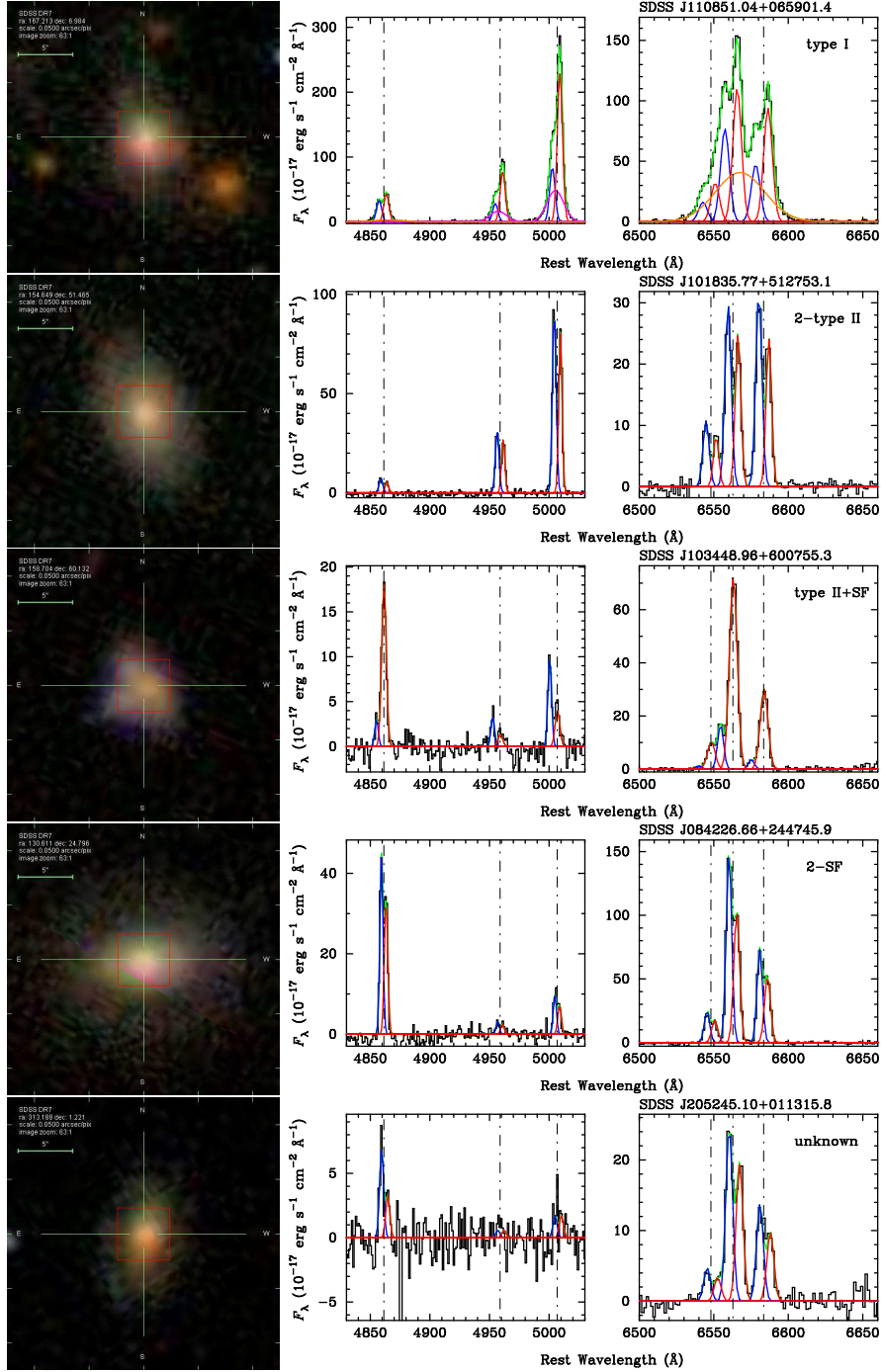


Fig. 5.— Image and spectrum examples of five kinds of *pp*-galaxies, showing the complicated double-peaked components.

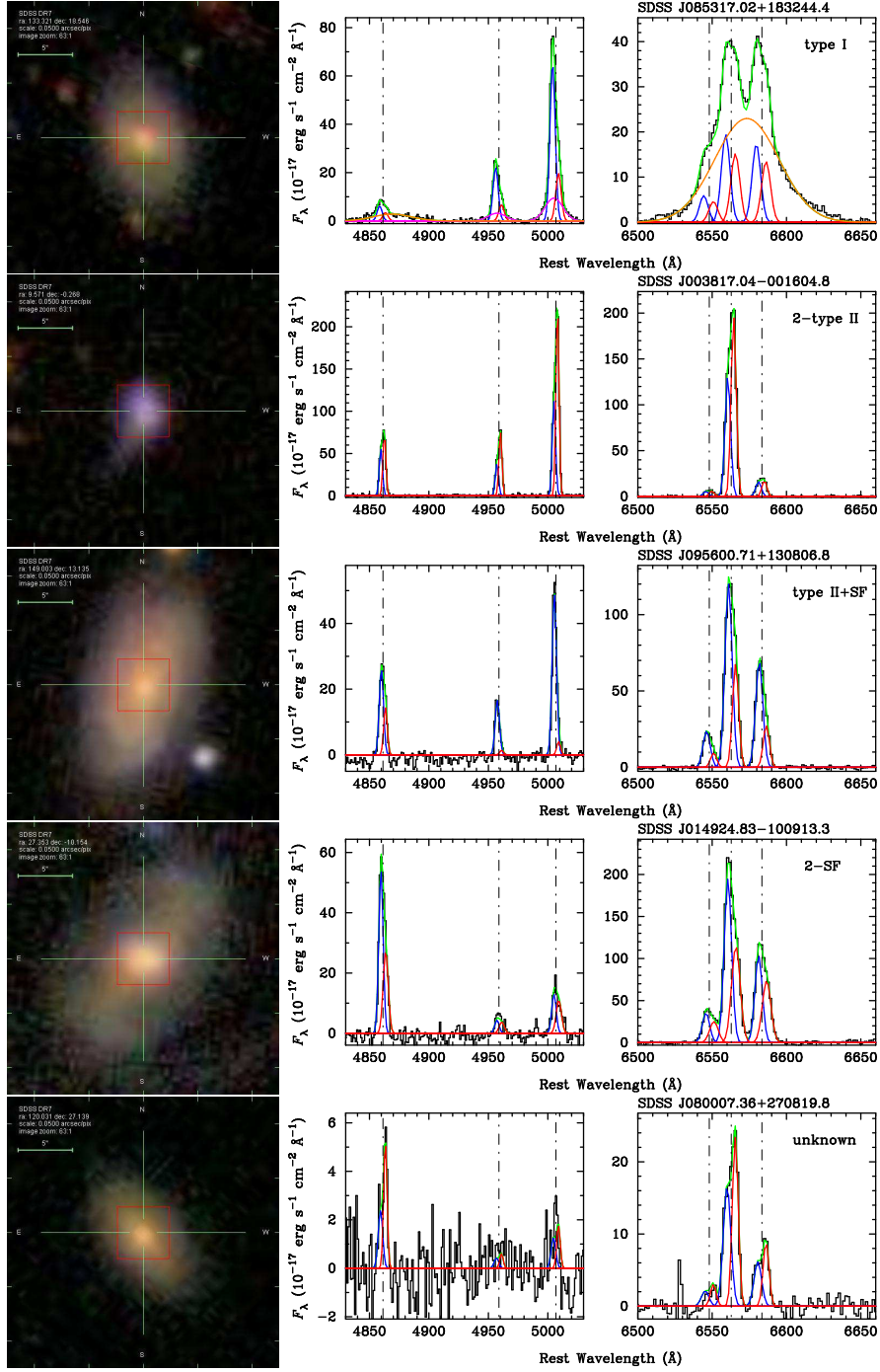


Fig. 6.— Image and spectrum examples of asym-NEL galaxies. They are candidates of *pp*-galaxies.

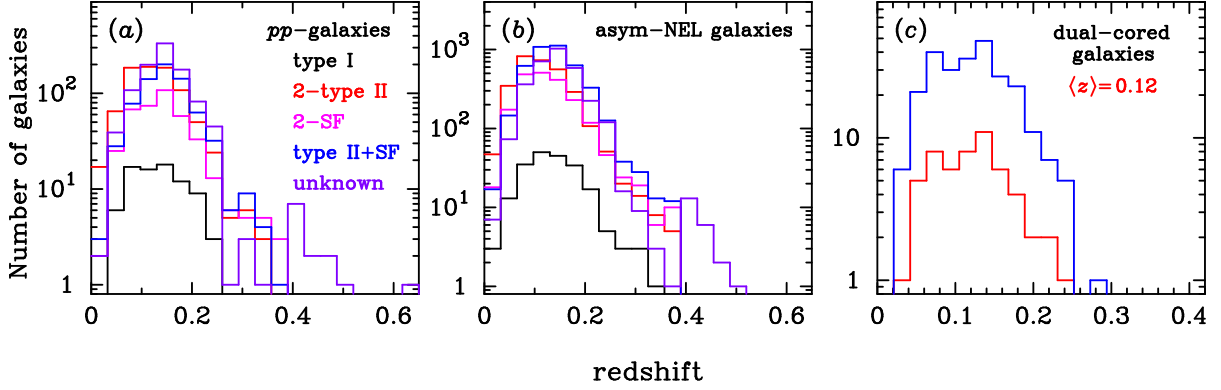


Fig. 7.— (a): The redshift distributions of the different kinds of pp -galaxies and (b) for asym-NEL galaxies; (c) for the 54 dual-cored galaxies (red line, with dual cores separated $< 3''$ listed in Table 6) along with the 255 dual-cored galaxies (the blue line, with dual cores separated $\geq 3''$ listed in Table 7).

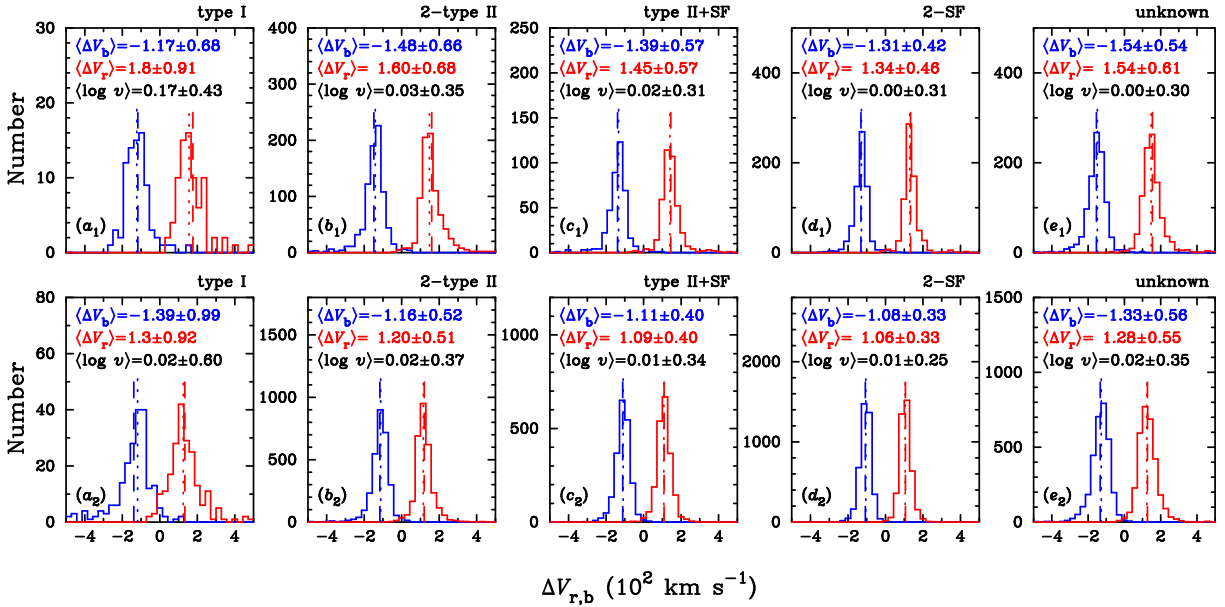


Fig. 8.— The shift distributions of the red and blue peaks of pp -galaxies (*top*) and asym-NEL galaxies (*bottom*). The blue line in each panel corresponds to the distribution of ΔV_b and the red line represent that of ΔV_r . In each panel, the blue dashed line represents the averaged blue shifts ($\langle \Delta V_b \rangle$) whereas the red dashed line stands for averaged red shifts ($\langle \Delta V_r \rangle$). The mean values (dashed line) are equal to the median values (dotted line) in these distributions. $\langle \log v \rangle = \langle \log |\Delta V_r / \Delta V_b| \rangle$ is the averaged logarithmic shift ratio of the red and blue components. Note that $\langle \Delta V_r \rangle$ and $\langle \Delta V_b \rangle$ given inside the panels are in units of 10^2 km s^{-1} .

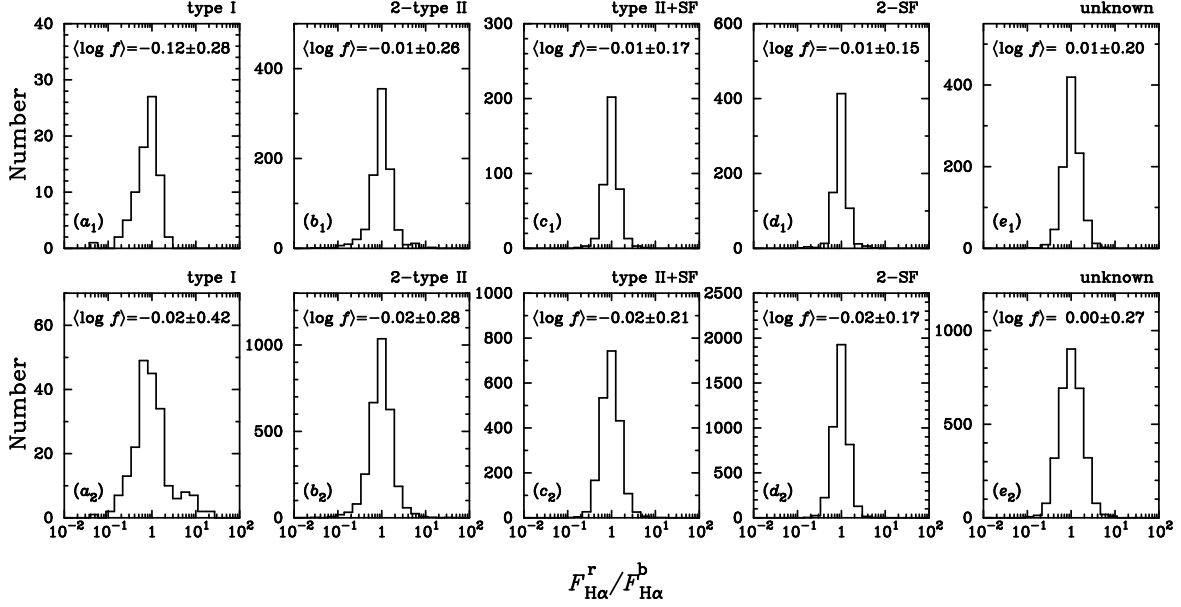


Fig. 9a.— The $\log(F_{\text{H}\alpha}^r/F_{\text{H}\alpha}^b)$ distributions. The upper panel is for pp -galaxies and lower panel for asym-NEL galaxies. The averaged values of the ratios are indicated in every plots. Here $\langle \log f \rangle = \langle \log(F_{\text{H}\alpha}^r/F_{\text{H}\alpha}^b) \rangle$.

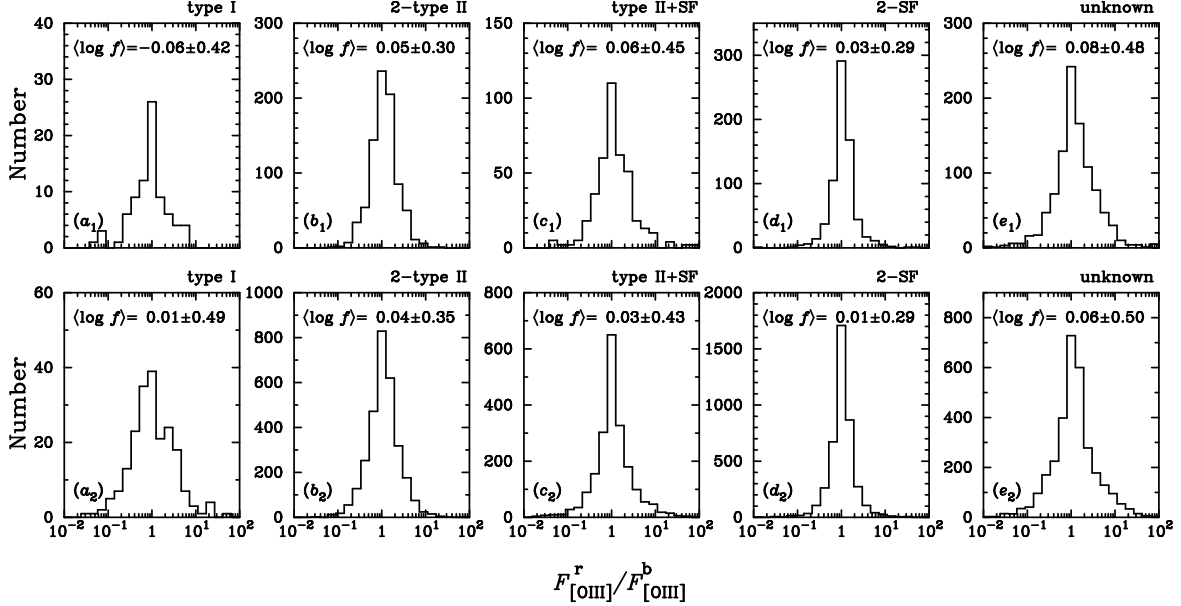


Fig. 9b.— The $\log(F_{[\text{O III}]}^r/F_{[\text{O III}]}^b)$ distributions. The upper panel is for pp -galaxies and lower panel for asym-NEL galaxies. Comparing the distributions, we find that distributions of $[\text{O III}]$ flux ratios are generally broader than $\text{H}\alpha$. Here $\langle \log f \rangle = \langle \log(F_{[\text{O III}]}^r/F_{[\text{O III}]}^b) \rangle$.

A. Monte-Carlo simulation of the selection criteria

Monte Carlo simulations have been performed in order to define the final selection criteria that allow us to maximally select potential galaxies with double-peaked narrow emission lines. According to the SDSS spectra resolution, we generate artificial spectra with a wavelength interval of 1\AA in the wavelength range of $[4950, 5050]\text{\AA}$ which only contains the [O III] $\lambda 5007$ narrow emission line. In order to show how the criteria depend on the spectral noise, we do the following two steps.

First, two Gaussian components are generated randomly to compose the [O III] $\lambda 5007$ emission line. Table 8 gives the simulated ranges of the parameters of the [O III] lines. For a random combination of the two components, double-peaked profiles do not necessarily appear in the composite spectra. However, it is easier to judge the presence of double-peaked profiles for a simulated noise-free spectrum. We search a critical wavelength point (λ_i) of the spectrum, where $F(\lambda_i)$ is smaller than its several neighbors at both sides, namely, $F(\lambda_{i-j}) > F(\lambda_i) < F(\lambda_{i+j})$, where $j = 1, 2, 3$. With the presence of λ_i , the spectrum is classified as an intrinsic double-peaked profile. Otherwise, it is a single-peaked spectrum. We generate many composed spectra (~ 1000) which are intrinsically double-peaked and noise-free.

Second, we examine if the produced spectra are double-peaked after adding noise to them. We generate two kinds of noisy spectra with $S/N = 10$ and $S/N = 30$. Through visual inspection, we select noisy spectra which show double-peaked profiles. We then fit these double-peaked spectra with the same methods as described in Section 2.2. We find that ~ 800 and ~ 900 can be selected as double-peaked objects from the 1,000 simulated-spectra. This means only 80% and 90% of the intrinsically double-peaked objects can be found for $S/N = 10$ and $S/N = 30$, respectively. The distributions of the parameters of double-peaked spectra yield the selection criteria.

We use three quantities ($\Delta V/\text{FWHM}_{\min}$, F_r/F_b) and S/N in the simulations, where $\Delta V = \Delta V_r - \Delta V_b$ is the velocity separation of the red and blue components, and FWHM_{\min} is the minimum of ($\text{FWHM}_{\text{red}}, \text{FWHM}_{\text{blue}}$). For a fixed S/N , we plot all the visually-selected double-peaked spectra in $F_r/F_b - \Delta V/\text{FWHM}_{\min}$ plane. Then the reasonable ranges of F_r/F_b and $\Delta V/\text{FWHM}_{\min}$ can be easily determined by the plane. Figure 10 *left* shows the simulations for two cases with $S/N = 10$ and $S/N = 30$, respectively.

Table 8. Monte-Carlo simulations: ranges of double-peaked [O III] lines

Parameters	ranges	notes
F_b/F_r	$[10^{-2}, 10^2]$	constrained by SDSS signal-noise ratio
V_b	$[-300, 0]\text{km s}^{-1}$	determined by the observed range
V_r	$[0, 300]\text{km s}^{-1}$	
$\text{FWHM}_{r,b}$	$[150, 700]\text{km s}^{-1}$	determined by SDSS spectral resolution
S/N	10 or 30	by SDSS signal-to-noise ratio

From Figure 10 *left* panel, we find that flux ratios beyond the range of [0.05, 20] can not be detected for $S/N = 30$. Therefore, we conservatively use flux ratios of [0.03, 30] in practice. Most double-peaked objects have $\Delta V/\text{FWHM}_{\min} > 1$. To make a proper complete automatic search, we use a criterion as $\Delta V/\text{FWHM}_{\min} > 0.8$.

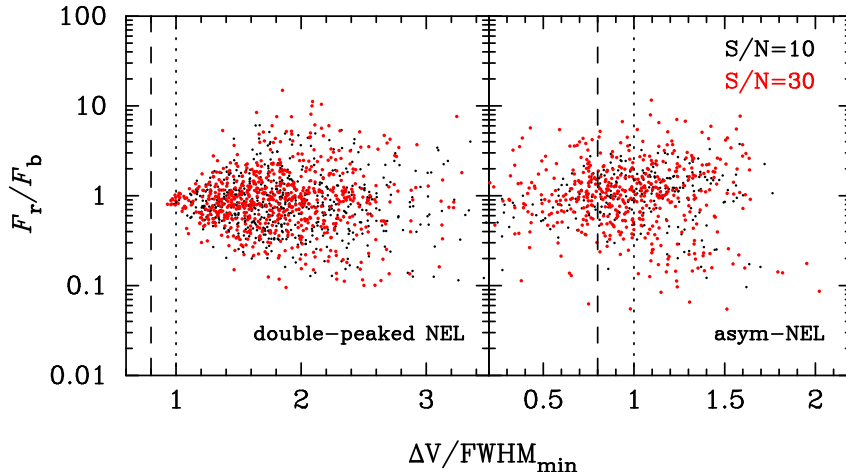


Fig. 10.— Monte Carlo simulation for the selection criteria of double-peaked, asymmetric and top-flat narrow emission lines with the same value of the parameters given by Table 8. The classifications of the simulated profiles are visually inspected. The black points represent the spectra with $S/N = 10$ and the red points correspond to $S/N = 30$. The vertical two lines represent $\Delta V/\text{FWHM}_{\min} = 0.8$ (dashed line) and 1.0 (dotted line). The *left* panel shows simulations for apparent double-peaked profiles of emission lines whereas the *right* panel for asym-NEL galaxies.

During the visual inspection of the simulated spectra, we find many asym-NEL sources which are referred to those sources without “trough”. We plot them in the *right* panel of Figure 10. The Monte-Carlo simulations for asym-NEL sources show that: 1) they have a similar range of F_r/F_b with double-peaked sources; 2) but they have different ranges of $\Delta V/\text{FWHM}_{\min}$. Therefore, the selected sources unavoidably cover many asym-NEL sources.

The present criteria guarantee the completeness of double-peaked sources. We emphasize that the criteria are only fit to selection of double-peaked sources rather than to the asym-NELs, but asym-NEL sources are selected as by-product of the criteria. For a goal of selecting a complete sample of asym-NEL galaxies, we have to define additional criteria for them, such as a definition of profile asymmetry, and try to find reasonable criteria. We will do this in a future paper. On the other hand, realistic distributions of parameters controlling the profiles listed in Table 8 are unknown, appearance of different kinds of profiles can not be predicted. It is thus hard for the Monte-Carlo simulations to predict the completeness of asym-NEL sources.

We also simulate the probability of mis-selection that single NELs could be selected as double-peaked or asym-NELs by our criteria. For $S/N=30$, only 2 of 10,000 are selected as asym-NEL sources, none as double-peaked sources whereas for $S/N=10$, only 1 as the double-peaked and 2 as the asym-NEL. It is clear that the fraction of mis-selected sources is very small.

B. Images and spectra of 54 dual-cored *pp*-galaxies and asym-NEL galaxies

The SDSS optical images and spectra of 54 dual-cored galaxies listed in Table 6 are shown in Figure 11.

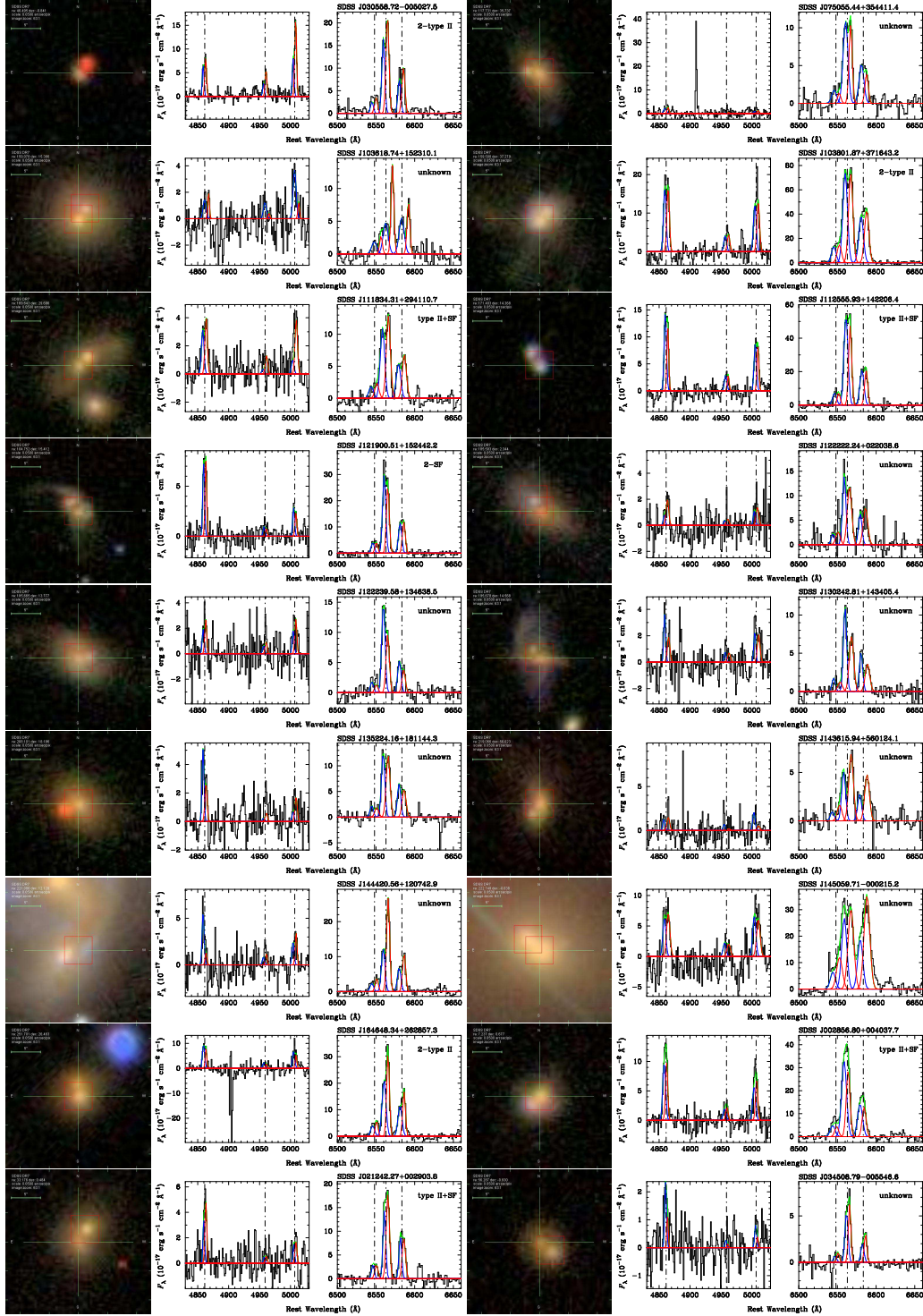


Fig. 11.— Images and spectra of 54 *pp*-galaxies and asym-NEL galaxies listed in Table 6. The name and type of the sources are labeled.

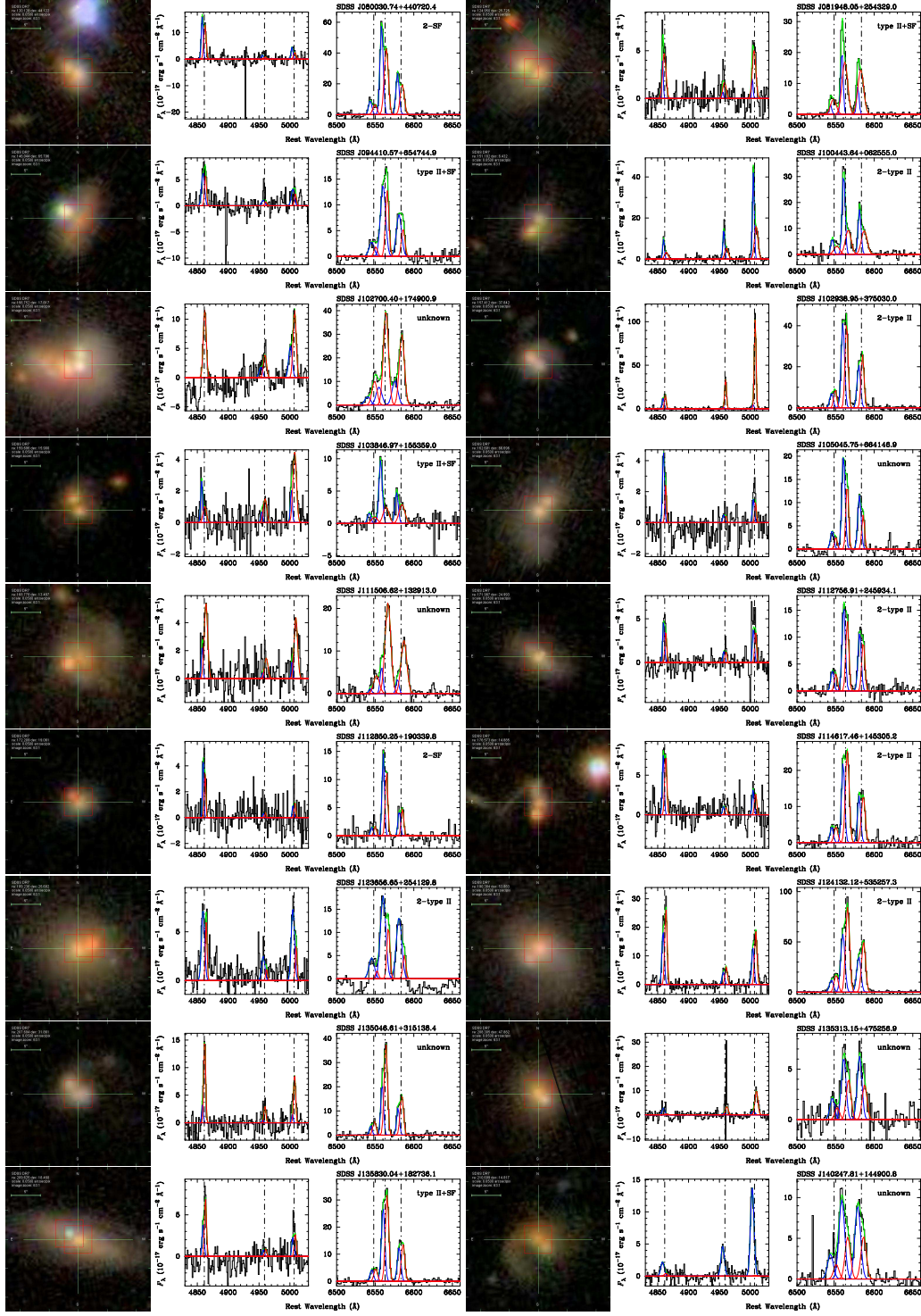


Fig. 11.— *Continued*

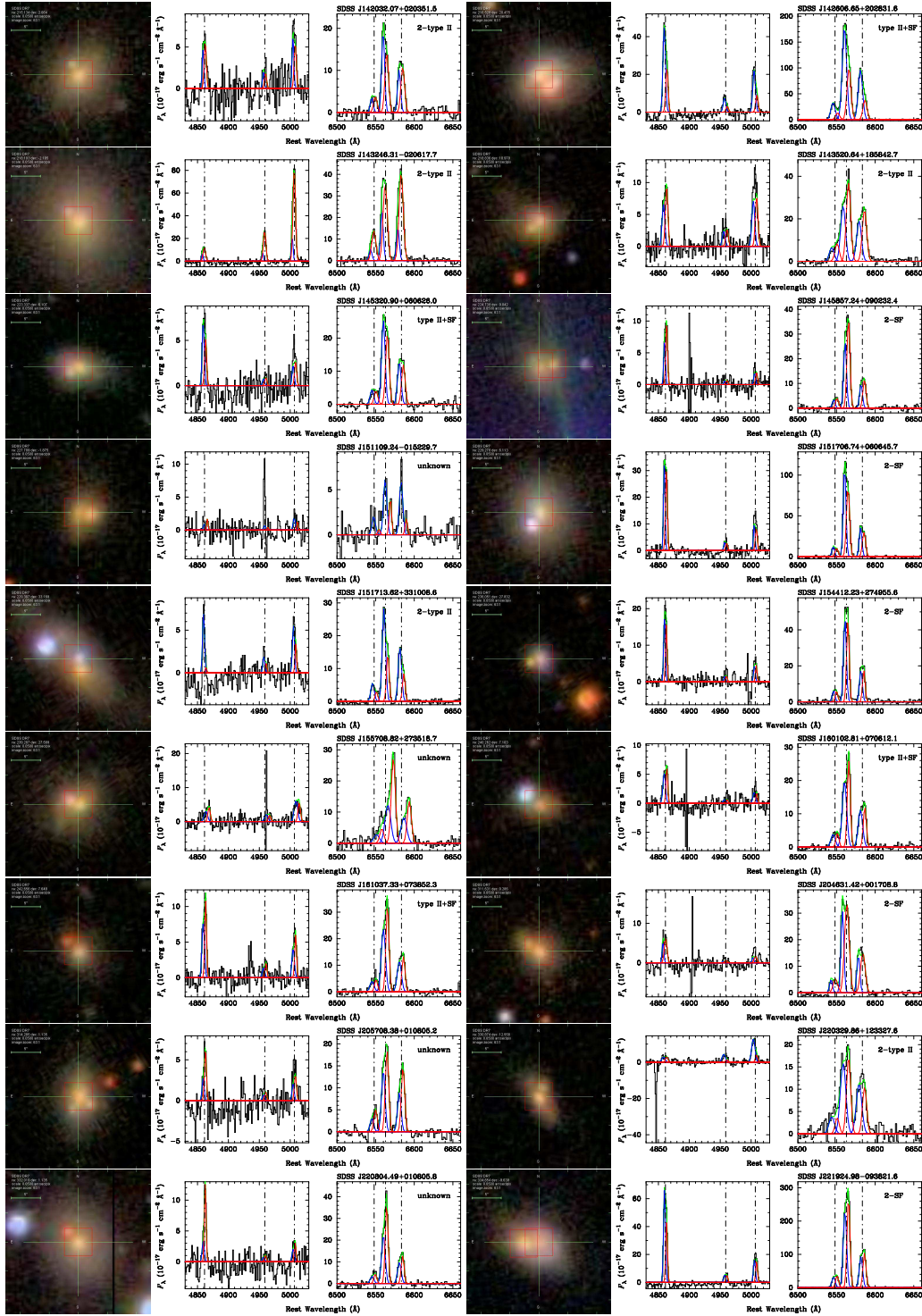


Fig. 11.— *Continued*

C. Images of 255 objects with double cores separated by $\geq 3''$

The SDSS optical images of the 255 dual-cored galaxies listed in Table 7 are shown in Figure 12.

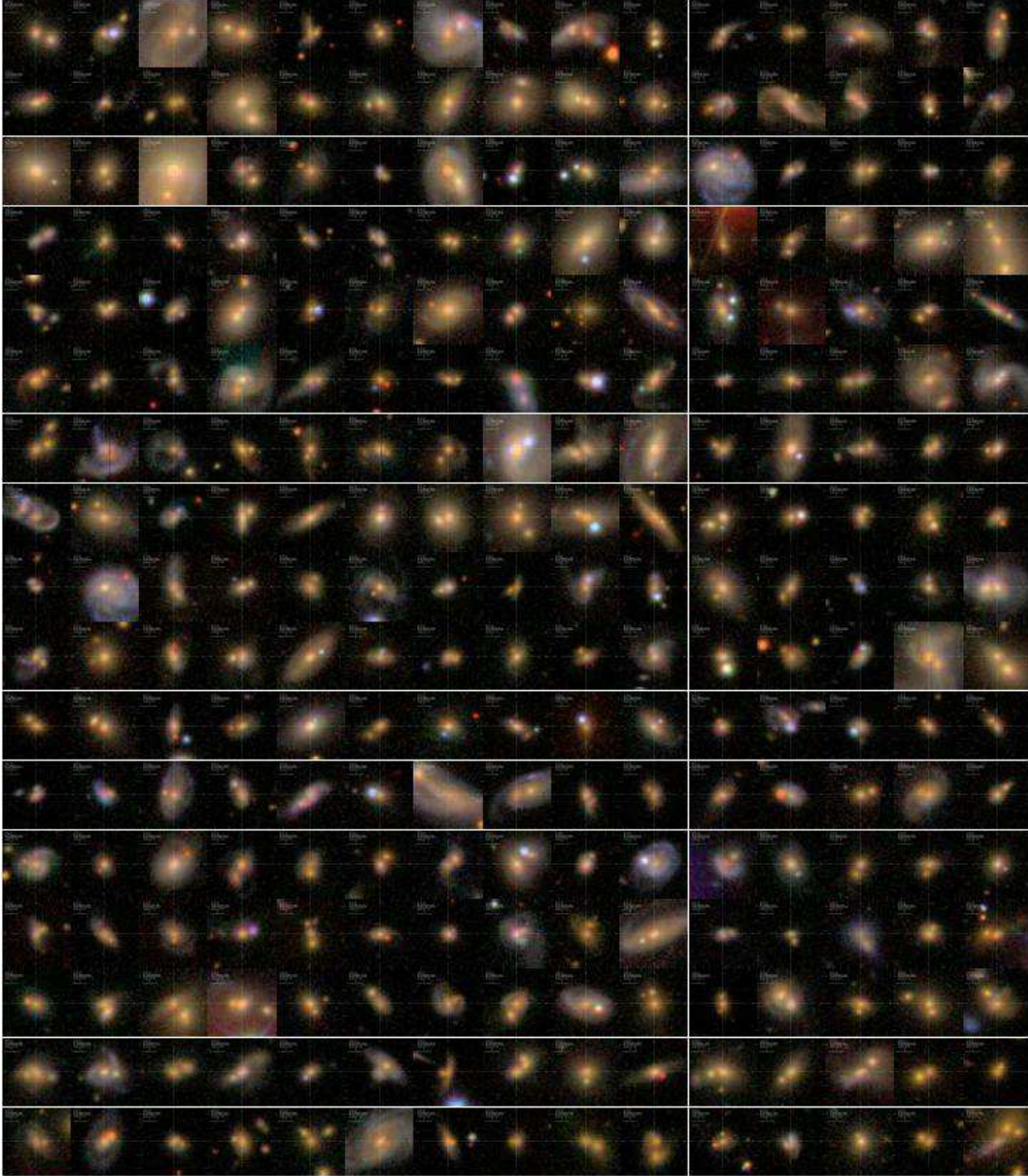


Fig. 12.— Image number can be obtained through $n = x + 15(y - 1)$, where $x = 1, 2, \dots, 15$ is a row number of an image from *left to right* and $y = 1, 2, 3, \dots, 17$ is a line number of an image from *top to below*. There are 15 images in each row. The number n corresponds to the number of objects listed in Table 7. No. $n = 1 - 67$ are those galaxies with double-peaked profiles, and $n = 68 - 255$ are ones with asymmetric or top-flat profiles. Each image has the same size of $25'' \times 25''$ and same orientations (i.e. up North, left East).